Fate of a strongly correlated *d*-wave superconductor in a Zeeman field: The Fulde-Ferrel-Larkin-Ovchinnikov perspective

Anushree Datta,[1] Kun Yang,[2] and Amit Ghosal[1,*]

[1]*Indian Institute of Science Education and Research Kolkata, Mohanpur 741246, India*
[2]*National High Magnetic Field Laboratory and Department of Physics, Florida State University, Tallahassee, Florida 32306, USA*

The Fulde-Ferrell-Larkin-Ovchinnikov (FFLO) phase is an unconventional superconducting state found under the influence of a strong Zeeman field. This phase is identified by finite center-of-mass momenta in the Cooper pairs, causing the pairing amplitude to oscillate in real space. Repulsive correlations, on the other hand, smear out spatial inhomogeneities in *d*-wave superconductors. We investigate the FFLO state in a strongly correlated *d*-wave superconductor within a consolidated framework of Hartree-Fock-Bogoliubov theory and the Gutzwiller approximation. We find that the crucial effects of strong correlations lie in shifting the BCS-FFLO phase boundary towards a lower Zeeman field and thereby enlarging the window of the FFLO phase. In the FFLO state, our calculation features a sharp midgap peak in the density of states, indicating the formation of strongly localized Andreev bound states. We also find that the signatures of the FFLO phase survive even in the presence of an additional translational-symmetry-breaking competing order in the ground state. This is demonstrated by considering a broken-symmetry ground state with a simultaneous presence of the *d*-wave superconducting order and a spin-density wave order, often found in unconventional superconductors.

I. INTRODUCTION

A magnetic field destroys superconductivity in two ways. One is through the orbital effect, which couples the magnetic field to the orbital motion of the electrons. This creates vortices in a superconductor by puncturing holes in the superconducting pairing amplitude, through which the magnetic flux lines penetrate. With increasing magnetic field, the density of the vortices increases and the pairing amplitude fails to recover between them, causing superconductivity to collapse progressively [1]. The second one is the Zeeman effect, where the magnetic field couples to the spin degrees of freedom of the electrons. This strains the spin-singlet configuration of the Cooper pairs owing to the split Fermi surfaces of spin-up and spin-down electrons. As the Zeeman field h, increases, a superconducting to normal state (NS) transition occurs at the Clogston-Chandrasekhar [2,3] limit, where the magnetization energy due to the Fermi surface splitting overcomes the condensation energy of the Cooper pairs. However, it was later shown that the Cooper pairs can survive beyond the Clogston-Chandrasekhar limit by having a finite pairing momentum, which can make the superconducting pairing amplitude spatially modulating, as proposed by Fulde and Ferrell [4] and by Larkin and Ovchinnikov independently [5]. The advantage of having spatially modulating pairing amplitude in a Zeeman field is to accommodate the magnetization in regions in which the pairing amplitude vanishes and thereby generating periodically inhomogeneous distribution of spatial order parameters. Hence, both the superconducting

pairing amplitude and the magnetization survive in the same system by periodically avoiding each other in space and the superconductivity is stabilized even at sufficiently large h. As a result, the system undergoes a transition from a usual BCS superconducting state at small h to a Fulde-Ferrell-Larkin-Ovchinnikov (FFLO) state at an intermediate range of h and finally to an NS at very high h.

Interestingly, a state with modulating pairing amplitude has also been proposed recently in the context of high-temperature cuprate superconductors, where the periodic inhomogeneity in pairing amplitude arises from strong electronic correlations in the underdoped regime of the cuprate phase diagrams. This phase is termed the pair-density wave (PDW) in the literature [6–10]. The modulations in pairing amplitudes in the FFLO and PDW phases are identical in nature. Their difference, however, lies in the fact that the FFLO phase breaks the time-reversal symmetry explicitly due to Zeeman effects, whereas the PDW does not necessarily break the time-reversal symmetry [11]. Naturally, the PDW state does not support a net magnetization either, unlike the FFLO phase [12]. In the present scenario, we only focus on the FFLO phase, where the generation of a spatially oscillating pairing amplitude is entirely due to the exposure to a Zeeman field.

The existence of the FFLO state had long been a theoretical truism [13–28], but it evaded experiments for many years. Two primary reasons behind this are the dominance of the orbital effect of applied magnetic field and the presence of disorder. The orbital effect, if dominant, often destroys superconductivity even before the appearance of the FFLO phase. The relative importance of the Zeeman effect and the orbital effect is characterized by the Maki parameter [29] $\alpha_M = \sqrt{2} H_{c_2}^{orb}(T=0)/H_p(T=0)$, where $H_{c_2}^{orb}$ is the orbital

*Corresponding author: ghosal@iiserkol.ac.in

critical field and H_p is the Pauli-limiting field. The orbital-limited materials, characterized by $\alpha_M < 1$, are thus unfavorable to conceive the FFLO phase. A modulating FFLO phase is generally believed to be extremely fragile in response to potential disorder [30,31], though there are recent studies that raise doubt on such inferences [32,33]. Despite these facts, the FFLO phase has gained renewed interest in recent times in the context of some unconventional superconductors. These include heavy-fermion superconductors such as CeCoIn$_5$ [34–45] and CeCu$_2$Si$_2$ [46], organic superconductors [47–57], Fe-based superconductors [58–60], and also cuprate superconductors [61–63]. Earlier, the possibility of the FFLO phase in cuprate superconductors attracted significant research endeavors. These are layered materials in which superconductivity is believed to arise in CuO$_2$ planes. Thus the magnetic field can be applied parallel to these planes to minimize orbital effects and couple only with the electronic spins [64]. However, their large H_p values obscure possibilities of realization of the FFLO phase [62]. The heavy-fermion superconductors are ideal for supporting this phase as they are Pauli-limited [65] and obtained in a reasonably clean form. Several experiments in CeCoIn$_5$ have indicated a modulating magnetic ordered state (coined the Q phase) in the presence of magnetic fields that survives only with superconductivity [39,44,66,67]. Note that the modulating pairing amplitude of the FFLO state also drives a spatial modulation in the magnetization. Therefore several proposals suggest that this magnetic order arises from the FFLO modulation [68–70], although there also exist other proposals for this observation [71–73]. More recently, nuclear magnetic resonance experiments on CeCu$_2$Si$_2$ [46] and the organic superconductor κ-(BEDT-TTF)$_2$Cu(NCS)$_2$ [47] have signaled the presence of Andreev bound states when magnetic fields were applied parallel to their conduction planes, one characteristic of the FFLO phase.

Most of these unconventional superconductors are prototypes of strongly correlated [74–81], quasi-2D superconductors [82,83]. Some of these superconductors, such as CeCoIn$_5$ and cuprates, also feature the d-wave symmetry in their superconducting energy gap [84,85]. In this work, we focus on exploring the effects of strong electronic correlations in a d-wave superconductor, exposed to a Zeeman field, with a perspective on the FFLO phase. Earlier theoretical studies on d-wave superconductors suggest that strong interactions change the nature and the degree of inhomogeneities and smear out the small-scale spatial charge fluctuations [86–88]. Strong correlations are thus expected to modify the existence or the nature of the FFLO phase, which exhibits periodic inhomogeneities in charge and spin densities. Moreover, the interplay of strong correlations with the magnetic field is also expected to uncover interesting physics. The effect of spin-dependent mass enhancement on the Fulde-Ferrell (FF) phase [4], the spatially homogeneous counterpart of the FFLO phase, has been studied recently [22].

We investigate the role of strong correlations in the FFLO state in a d-wave superconductor within an integrated framework of Hartree-Fock-Bogoliubov theory and the Gutzwiller approximation. The crux of our findings is as follows: (i) At $T = 0$, near the optimal doping for superconductivity, strong correlations renormalize the different energy scales of the system. As a result, their subtle balance shifts the

boundaries of the FFLO phase, and consequently, it increases the FFLO window of the Zeeman field. (ii) The behaviors of the order parameters and the pairing momenta in the presence and absence of strong correlations are contrasting in nature owing to the renormalizations of different parameters in the Hamiltonian. (iii) Strong correlations cause a sharper and narrower midgap peak appearing at the density of states in the FFLO phase. This is due to a strong localization of the Andreev bound states at regions having zero pairing amplitude owing to its sharp sign change near those regions. (iv) The signature of the FFLO phase survives even when the $h = 0$ ground state (GS) has competing orders. We show this by considering a GS that has a competing spin-density wave (SDW) order in addition to the d-wave BCS order.

The rest of the paper is organized as follows: In Sec. II we give the details of the model used in our calculations emphasizing the way the effects of strong correlations are introduced through Gutzwiller factors. We also discuss the computational method of our study at $T = 0$. In Secs. III A–III D we present our results in which we compare the phase diagrams, the behavior of the parameters, and the observables with respect to the applied magnetic field in the presence and absence of strong correlations. In Sec. III E we discuss the phase diagrams in the presence of an additional competing SDW order. Finally, we conclude in Sec. IV.

II. MODEL AND METHODS

We describe our system by the microscopic Hubbard Hamiltonian:

$$\mathcal{H}_{\text{Hub}} = -t \sum_{\langle ij \rangle \sigma} (\hat{c}_{i\sigma}^\dagger \hat{c}_{j\sigma} + \text{H.c.}) + U \sum_i \hat{n}_{i\uparrow} \hat{n}_{i\downarrow}. \quad (1)$$

Here, t is the hopping energy of the electrons to its nearest neighbors, denoted as $\langle ij \rangle$, on a 2D square lattice, and U is the on-site repulsion energy between the electrons. In the strongly correlated limit $U \gg t$, an effective low-energy Hamiltonian can be obtained from $\mathcal{H}_{\text{Hub}}$ that lives in a restricted Hilbert space that prohibits double occupancy of any site due to strong on-site repulsions. The resulting Hamiltonian is known as the t-J model, which can be considered as the perturbative expansion of $\mathcal{H}_{\text{Hub}}$ up to the quadratic order in t/U:

$$\mathcal{H}_{t-J} = -t \sum_{\langle ij \rangle \sigma} (\tilde{c}_{i\sigma}^\dagger \tilde{c}_{j\sigma} + \text{H.c.}) + J \sum_{\langle ij \rangle} \left(\tilde{\mathbf{S}}_\mathbf{i} \cdot \tilde{\mathbf{S}}_\mathbf{j} - \frac{\tilde{n}_\mathbf{i} \tilde{n}_\mathbf{j}}{4} \right). \quad (2)$$

Here, the exchange interaction $J = 4t^2/U$ emerges via Schrieffer-Wolff transformation. The renormalized creation operator $\tilde{c}_{i\sigma}^\dagger = (1 - \hat{n}_{i\bar{\sigma}})\hat{c}_{i\sigma}^\dagger$ is defined to operate on the Hilbert space that excludes all double occupancies. In order to probe the FFLO state, we introduce the Zeeman field h and redefine $\mathcal{H}_{t-J}$ as $\mathcal{H}_{t-J} - \sum_{i\sigma} \sigma h \hat{n}_{i\sigma}$. Analyzing the Hamiltonian in Eq. (2) is challenging due to the projection operators that are usually dealt with using variational quantum Monte Carlo methods [89]. A simpler implementation of the projections is achieved through a Gutzwiller approximation (GA) [90], an approximation method that incorporates the Hilbert-space restrictions in a spirit similar to that of a mean-field theory. Within the framework of the GA, we write the GS wave

function as $|\psi\rangle = \Pi_i (1 - \hat{n}_{i\uparrow}\hat{n}_{i\downarrow})|\psi_0\rangle$, where $|\psi_0\rangle$ is the GS wave function in the unrestricted Hilbert space. In GA, the effects of projection are mimicked in Gutzwiller renormalization factors (GRFs) [91] represented as $g_{ij}^{t,\sigma}$, $g_{ij}^{J,z}$, $g_{ij}^{J,xy}$, which depend on the local densities, magnetization, pairing amplitude, and kinetic energies. The explicit expressions of the Gutzwiller factors are provided in Appendix A 1. Finally, using GA, the Hamiltonian for strongly correlated d-wave superconductors in a Zeeman field is shaped as

$$
\mathcal{H}_{\rm GA} = -t \sum_{\langle ij\rangle\sigma} g_{ij}^{t\sigma}(\hat{c}_{i\sigma}^\dagger \hat{c}_{j\sigma} + {\rm H.c.}) - \sum_{i\sigma} \sigma h \hat{n}_{i\sigma}
$$
$$
+ J \sum_{\langle ij\rangle}\left[g_{ij}^{J,z}\hat{S}_i^z\hat{S}_j^z + g_{ij}^{J,xy}\left(\frac{\hat{S}_i^+\hat{S}_j^- + \hat{S}_i^-\hat{S}_j^+}{2}\right) - \frac{\hat{n}_i\hat{n}_j}{4}\right].
$$
(3)

We define our local order parameters as follows:

$$
\Delta_{ij\sigma} = \sigma\langle\psi_0|\hat{c}_{i\sigma}\hat{c}_{j\bar{\sigma}}|\psi_0\rangle, \tag{4}
$$

$$
\tau_{ij\sigma} = \langle\psi_0|\hat{c}_{i\sigma}^\dagger\hat{c}_{j\sigma}|\psi_0\rangle, \tag{5}
$$

$$
n_{i\sigma} = \langle\psi_0|\hat{c}_{i\sigma}^\dagger\hat{c}_{i\sigma}|\psi_0\rangle, \quad m_i = \frac{1}{2}\sum_\sigma \sigma n_{i\sigma}. \tag{6}
$$

Using the above order parameters, the mean-field decomposition of $\mathcal{H}_{\rm GA}$ in Hartree, Fock, and Bogoliubov channels, whose details are provided in Appendix A 2, leads to

$$
\mathcal{H}_{\rm MF} = \sum_{i\alpha\sigma}\left[-tg^{t\sigma} - \frac{J}{2}g^{xy}\tau_{\bar\sigma} - \frac{J}{4}(g^z-1)\tau_\sigma + \Gamma_{i\sigma}^\alpha\right]\hat{c}_{i\sigma}^\dagger\hat{c}_{i+\alpha\sigma}
$$
$$
+ \sum_{i\alpha}\left\{\left[-\frac{J}{2}g^{xy}\Delta_{i\downarrow}^\alpha - \frac{J}{4}(g^z+1)\Delta_{i\uparrow}^\alpha\right]\hat{c}_{i\uparrow}^\dagger\hat{c}_{i+\alpha\downarrow}^\dagger + {\rm H.c.}\right\}
$$
$$
- \sum_{i\alpha}\left[(\theta_{i\uparrow}^\alpha\hat{c}_{i\uparrow}^\dagger\hat{c}_{i+\alpha\downarrow}^\dagger + \theta_{i\downarrow}^\alpha\hat{c}_{i+\alpha\uparrow}^\dagger\hat{c}_{i\downarrow}^\dagger) + {\rm H.c.}\right]
$$
$$
+ \sum_{i\alpha\sigma}\frac{J}{4}[(g^z-1)n_{i+\alpha\sigma} - (g^z+1)n_{i+\alpha\bar\sigma}]\hat{n}_{i\sigma}
$$
$$
+ \sum_{i\sigma}(\phi_{i\sigma} - \mu_\sigma)\hat{n}_{i\sigma}, \tag{7}
$$

where the notations $g^{t\sigma}$, g^{xy}, g^z, μ_σ, τ_σ, $\tau_{\bar\sigma}$ are abbreviations corresponding to $g_{i,i+\alpha}^{t\sigma}$, $g_{i,i+\alpha}^{J,xy}$, $g_{i,i+\alpha}^{J,z}$, $\mu + \sigma h$, $\tau_{i,i+\alpha\sigma}$, $\tau_{i,i+\alpha\bar\sigma}$, respectively. Here, $\Gamma_{i\sigma}^\alpha$, $\theta_{i\sigma}^\alpha$, and $\phi_{i\sigma}$ subsume the terms involving the derivatives of GRFs in $\partial W/\partial\tau_{i,i+\alpha\sigma}$, $\partial W/\Delta_{i\sigma}^\alpha$, and $\partial W/\partial n_{i\sigma}$, respectively, where $W = \langle\psi_0|\mathcal{H}_{\rm GA}|\psi_0\rangle - \lambda(\langle\psi_0|\psi_0\rangle - 1) - \mu(\sum_i n_i - \langle n\rangle)$, and α stands for nearest-neighbor spacings from i. Here, λ is a Lagrange multiplier fixing the wave-function renormalization $\langle\psi_0|\psi_0\rangle = 1$, and μ is the chemical potential that takes care of the average density $\langle n\rangle = N^{-1}\sum_i n_i$ of the system. In this work, we focus on the d-wave symmetry of the local superconducting pairing amplitude, defined as $\Delta_i = \sum_\sigma(\Delta_{i,\sigma}^{+\hat{x}} + \Delta_{i,\sigma}^{-\hat{x}} - \Delta_{i,\sigma}^{+\hat{y}} - \Delta_{i,\sigma}^{-\hat{y}})/4$. A closely related pairing anisotropy is the local extended s-wave pairing amplitude, defined as $\Delta_i^{\rm xs} = \sum_\sigma(\Delta_{i,\sigma}^{+\hat{x}} + \Delta_{i,\sigma}^{-\hat{x}} + \Delta_{i,\sigma}^{+\hat{y}} + \Delta_{i,\sigma}^{-\hat{y}})/4$; however, we choose model parameters for which the strength of $\Delta_i^{\rm xs}$ is negligible (see Appendix B for details). To gauge the effects of strong correlations, we compare two sets of results

obtained in the presence and absence of strong correlations. In the presence of strong correlations, we rely on the framework based on the Gutzwiller approximation augmented with Hartree-Fock-Bogoliubov theory, as discussed already, whereas in the absence of strong correlations, we employ Hartree-Fock-Bogoliubov theory on the unrestricted Hilbert space, i.e., without any double-occupancy prohibition. Operationally, this is equivalent to setting the Gutzwiller factors to unity. We will use the notation IMT (inhomogeneous mean-field theory) to refer to the calculation based on Hartree-Fock-Bogoliubov theory, and RIMT (renormalized inhomogeneous mean-field theory) to refer to the scheme based on Hartree-Fock-Bogoliubov theory and the Gutzwiller approximation in our discussions from now on. We set $U = 12t$ for RIMT [92], and choose $U = 3.077t$ and set the Gutzwiller factors to unity for IMT. This yields the same d-wave superconducting gap at $h = 0$ in these two schemes. We place $\langle n\rangle$ at 0.84, a value that ensures a pristine superconducting state away from the dominance of the competing orders. For example, such $\langle n\rangle$ value is known as the optimal doping for cuprate superconductors. This is convenient for our case, since the primary motivation here is to study the effects of strong correlations in the FFLO phase, i.e., a superconducting phase with finite-momentum Cooper pairs. However, it is also interesting to study the effects in the presence of competing orders, which we will discuss later in Sec. III E. In our investigation, we will focus on the Larkin-Ovchinnikov (LO) state in which the pairing profile in the lattice is $\Delta_i \approx 2\Delta_q\cos(\mathbf{q}\cdot\mathbf{r}_i)$. Here, $\mathbf{q}$ is the pairing momentum of the Cooper pairs and $\mathbf{r}_i$ denotes the position of the ith lattice site. Such a behavior of the pairing amplitude arises due to the coupling of the single-particle states $|\mathbf{k},\sigma\rangle$ with both $|-\mathbf{k}+\mathbf{q},\bar\sigma\rangle$ and $|-\mathbf{k}-\mathbf{q},\bar\sigma\rangle$. The states $|-\mathbf{k}+\mathbf{q},\bar\sigma\rangle$ and $|-\mathbf{k}-\mathbf{q},\bar\sigma\rangle$ also connect to $|\mathbf{k}+2\mathbf{q},\sigma\rangle$ and $|\mathbf{k}-2\mathbf{q},\sigma\rangle$, respectively, in the Cooper channel. This links the single-particle state $|\mathbf{k},\sigma\rangle$ with the states $|\mathbf{k}\pm 2\mathbf{q},\sigma\rangle$, $|\mathbf{k}\pm 4\mathbf{q},\sigma\rangle$, and so on with progressive weaker coupling. Subsequently, an intertwined spin-density wave (SDW) order and a charge-density wave (CDW) order are generated with modulating wave vectors $2\mathbf{q}$, $4\mathbf{q}$, etc., which seeds many intriguing consequences in the presence of strong electronic correlations. Note that allowing only FF [4] pairing ($\Delta_i = \Delta_q e^{i\mathbf{q}\cdot\mathbf{r}_i}$) does not generate any such SDW or CDW order. We finally solve the mean-field Hamiltonian in the momentum space, owing to the periodic inhomogeneity in the FFLO phase. Drawing from the above discussions, the spatial profile of spin densities looks like

$$
n_{i\sigma} = n_0^\sigma + 2n_{2q}^\sigma\cos(2\mathbf{q}\cdot\mathbf{r}_i) + 2n_{4q}^\sigma\cos(4\mathbf{q}\cdot\mathbf{r}_i) + \cdots, \tag{8}
$$

where $n_Q^\sigma = N^{-1}\sum_k\langle\hat{c}_{k+Q\sigma}^\dagger\hat{c}_{k\sigma}\rangle_0$, where $Q = 0$, $\pm 2q$, $\pm 4q$ and so on. Here, $\langle\cdots\rangle_0$ signifies expectation value with respect to the unprojected wave function $|\psi_0\rangle$. As the GRFs are functions of local spin densities, we fuse the following ansatz for them:

$$
g_{i,i+\alpha}^{t\sigma} = g_0^{t\sigma} + 2g_{2\mathbf{q}\alpha}^{t\sigma}\cos(2\mathbf{q}\cdot r_i) + 2g_{4\mathbf{q}\alpha}^{t\sigma}\cos(4\mathbf{q}\cdot r_i) + \cdots, \tag{9}
$$

$$
g_{i,i+\alpha}^{J,\nu} = g_0^{J,\nu} + 2g_{2q\alpha}^{J,\nu}\cos(2\mathbf{q}\cdot\mathbf{r}_i) + 2g_{4q\alpha}^{J,\nu}\cos(4\mathbf{q}\cdot\mathbf{r}_i) + \cdots, \tag{10}
$$

where $\nu = xy$ or z. Using the periodic translational symmetry of this phase, we solve Eq. (7) in the momentum space. We take the spin densities up to n_{4q}^σ mode, pairing amplitude up to Δ_{3q} (which along with the higher-order modes also arise naturally with a weaker coupling as a result of the connected chains of single-particle states), and neglect the higher-order modes to simplify our calculations. We have checked our results by considering the higher-order modes in the spin densities and the pairing amplitude in our Gutzwiller mean-field theory calculations, and our results indicate that their effects are minimal in determining the phase boundaries and the important features of the physical observables we have studied here.

Building on these ideas, $\mathcal{H}_{MF}$ in the momentum space becomes

$$\mathcal{H}_{MF} = \sum_{k,Q,\sigma} \xi_{k+Q\sigma}^{(r)} \hat{c}_{k\sigma}^\dagger \hat{c}_{k+Q\sigma}$$
$$+ \sum_{k,Q_p} \left(\Delta_{k,-k+Q_p}^{(r)} \hat{c}_{k\uparrow}^\dagger \hat{c}_{-k+Q_p\downarrow}^\dagger + \text{H.c.} \right). \quad (11)$$

Here, $Q = 0, \pm 2q, \pm 4q$, and $Q_p = \pm q, \pm 3q$. The explicit expressions of $\xi_{k+Q\sigma}^{(r)}$ and $\Delta_{k,-k+Q_p}^{(r)}$ and the self-consistent equations of the order parameters are given in Appendix A 3. The Hamiltonian in Eq. (11) can be written in Nambu space as

$$\mathcal{H}_{MF} = \Psi^\dagger \hat{H}_{MF} \Psi. \quad (12)$$

Here, $\hat{H}_{MF}$ is a $2N \times 2N$ matrix, which has the form

$$\hat{H}_{MF} = \begin{bmatrix} \hat{\xi}_{kp\sigma} & \hat{\Delta}_{kp} \\ \hat{\Delta}_{kp}^* & -\hat{\xi}_{kp\bar{\sigma}}^* \end{bmatrix}, \quad (13)$$

where the $\hat{\xi}_{kp\sigma}$, $\hat{\Delta}_{kp}$ components of the $N \times N$ matrices (k and p both take up N values) are expressed as follows:

$$\hat{\xi}_{kp\sigma} = \delta_{kp} \xi_{p\sigma}^{(r)} + \delta_{k+Q,p} \xi_{p\sigma}^{(r)}, \quad (14)$$

$$\hat{\Delta}_{kp} = \delta_{-k+Q_p,p} \Delta_{kp}^{(r)}, \quad (15)$$

$$\Psi^\dagger = \left[\hat{c}_{k_1\sigma}^\dagger, \ldots, \hat{c}_{k_N\sigma}^\dagger, \hat{c}_{k_1\bar{\sigma}}, \ldots, \hat{c}_{k_N\bar{\sigma}} \right]. \quad (16)$$

Here, $N = L \times L$ indicates the total number of sites in the lattice, with L being the length of the same. We exploit the translational symmetry of the system and block-diagonalize $\hat{H}_{MF}$ in Eq. (13) into smaller matrices. A typical size of the block is $2L \times 2L$, which can be further reduced depending on the periodicity of the order parameters in the lattice. Most of our calculations are for $L = 200$, except the results shown in real space, which are for $L = 40$. We diagonalize the resulting Hamiltonian using the transformations $\hat{c}_{k\sigma} = \sum_n (u_{k,n\sigma} \gamma_{n\sigma} - \sigma v_{k,n\sigma}^* \gamma_{n\bar{\sigma}}^\dagger)$, where $\gamma_{n\sigma}$ and $\gamma_{n\bar{\sigma}}^\dagger$ are Bogoliubov quasiparticle operators and $u_{k,n\sigma}$ and $v_{k,n\bar{\sigma}}$ satisfy the equation

$$\sum_p \begin{bmatrix} \hat{\xi}_{kp\sigma} & \hat{\Delta}_{kp} \\ \hat{\Delta}_{kp}^* & -\hat{\xi}_{kp\bar{\sigma}}^* \end{bmatrix} \begin{bmatrix} u_{p,n\sigma} \\ v_{p,n\bar{\sigma}} \end{bmatrix} = E_{n\sigma} \begin{bmatrix} u_{k,n\sigma} \\ v_{k,n\bar{\sigma}} \end{bmatrix}. \quad (17)$$

The Hamiltonian in Eq. (11) in the presence of the Zeeman field describes the d-wave BCS, FFLO, and spin-polarized NS phases, as well as CDW or SDW order and interplay among these in the GS.

As mentioned earlier, we will also present some of the results in real space in Secs. III A, III B, and III E, for which we use Bogoliubov–de Gennes (BdG) transformations [93], $\hat{c}_{i\sigma} = \sum_n (\gamma_{n\sigma} u_{i,n\sigma} - \sigma \gamma_{n\bar{\sigma}}^\dagger v_{i,n\sigma}^*)$, for diagonalizing Eq. (7). This results in the following eigenequation,

$$\sum_j \begin{bmatrix} \hat{\xi}_{ij\sigma} & \hat{\Delta}_{ij} \\ \hat{\Delta}_{ji}^* & -\hat{\xi}_{ij\bar{\sigma}}^* \end{bmatrix} \begin{bmatrix} u_{j,n\sigma} \\ v_{j,n\bar{\sigma}} \end{bmatrix} = E_{n\sigma} \begin{bmatrix} u_{i,n\sigma} \\ v_{i,n\bar{\sigma}} \end{bmatrix}, \quad (18)$$

which is self-consistently solved for all the local order parameters defined in Eqs. (4), (5), and (6). The matrix equation in Eq. (18) leads to the following equations,

$$\hat{\xi}_{ij\sigma} = \left[-t g_{ij}^{t\sigma} - \frac{J}{2} g_{ij}^{J,xy} \tau_{ij\bar{\sigma}} - \frac{J}{4} (g_{ij}^{J,z} - 1) \tau_{ij\sigma} + \Gamma_{ij\sigma} \right] \delta_{i+\alpha,j}$$
$$- \sum_\alpha \frac{J}{2} \left[(g_{i,i+\alpha}^{J,z} + 1) n_{i+\alpha\bar{\sigma}} - (g_{i,i+\alpha}^{J,z} - 1) n_{i+\alpha\sigma} \right] \delta_{i,j}$$
$$+ (\phi_{i\sigma} - \mu_\sigma) \delta_{i,j}, \quad (19)$$

$$\hat{\Delta}_{ij} = \left[-J g_{ij}^{J,xy} \Delta_{ij\downarrow} - \frac{J}{2} (g_{ij}^{J,z} + 1) \Delta_{ij\uparrow} - \theta_{ij\uparrow} \right] \delta_{i+\alpha,j}. \quad (20)$$

Diagonalizing the BdG matrix in Eq. (18) is numerically expensive. So, we solve the BdG matrix to obtain the real-space pictures only for $L = 40$. Considering smaller systems comes with an energy cost for the FFLO state, as it puts constraint on the possible q values for the variational determination of the lowest-energy state.

III. RESULTS

In the following we discuss the fate of the FFLO phase due to strong correlations at $T = 0$ by contrasting the behavior of different observables obtained within RIMT and IMT calculations.

A. Phase diagram

Earlier theoretical studies on superconductors subjected to a Zeeman field h suggest that a BCS superconductor with spatially uniform pairing amplitude undergoes a phase transition to an FFLO phase with a periodically modulated order parameter at $h = h_1$. Upon increasing h further, superconductivity gets fully suppressed for $h \geqslant h_2$ (here, $h_2 > h_1$), leading to a spin-polarized normal state (NS) [13,17,20,32,61,94–96]. The FFLO phase is thus sandwiched between a uniform BCS (for low $h \leqslant h_1$) and a spin-polarized NS (at large $h \geqslant h_2$). These three phases are identified by blue, pink, and white shades in Fig. 1 (and also later in Figs. 2, 3, 6, 12, 13). These phases are realized in our calculations as the GS for different h values within the framework of a Hartree-Fock-Bogoliubov description of $\mathcal{H}_{t-J}$, in both RIMT and IMT calculations. The location of the phase boundaries, i.e., the values of h_1 and h_2, differ from the two methods of calculations, as shown in Fig. 1. The differences arise because of the physics of strong electronic correlations captured by the RIMT method, as we proceed to discuss below.

We identify the GS by considering the possible broken-symmetry solutions, and then choosing the one with the lowest energy as shown in the main panel of Fig. 1. We find that the introduction of the Gutzwiller factors lowers h_1
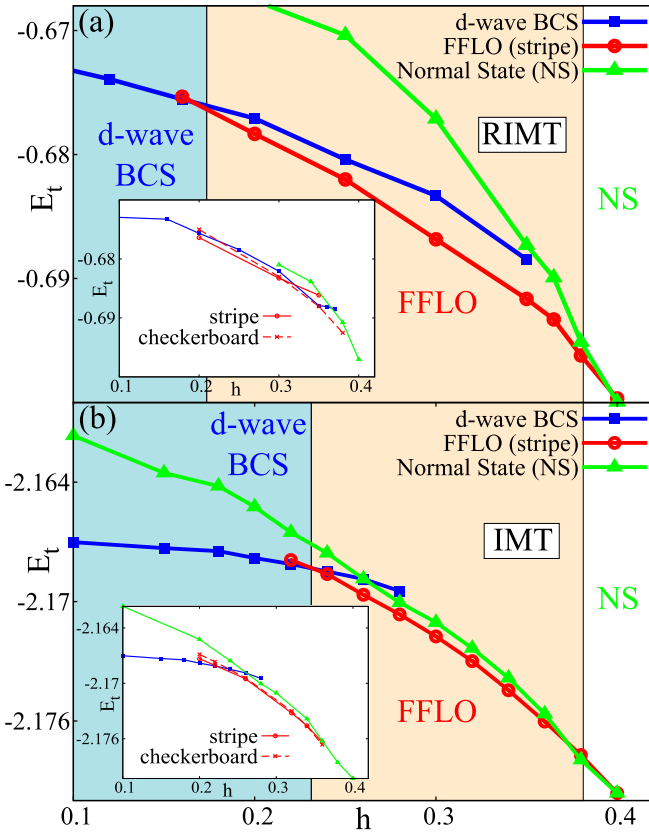
FIG. 1. Energetics of ground states with h for different broken symmetries, calculated within RIMT (a) and IMT (b) methods (see Sec. II for model parameters). A d-wave BCS state (blue curve), an FFLO state (red curve) and a normal state (green curve) are considered for comparison. Though the FFLO ground state is found sandwiched between the d-wave BCS state (low h) and the normal state (large h) both in RIMT and IMT, it is realized in a wider range of $0.18 \leqslant h \leqslant 0.38$ in RIMT findings (a) than that from IMT (b) window of $0.22 \leqslant h \leqslant 0.38$. We mark the FFLO and BCS regions by pink and blue shades, respectively. The inset in each panel shows that the nature of modulations of the superconducting pairing amplitude within the FFLO phase changes from a stripe to a checkerboard form (see Sec. III A for details). Such a changeover occurs at $h \approx 0.25$ in the RIMT calculation (a) and at $h \approx 0.33$ in the IMT scheme (b).

(while keeping h_2 more or less unaltered) and thus enhances the window of stability of the FFLO GS. In particular, for our model parameters, i.e., $J/t = 0.33$ and average density $\langle n \rangle = 0.84$, we obtain $h_1 \approx 0.18$ and $h_2 \approx 0.38$ (expressed in units of t) by the RIMT method in Fig. 1(a). In contrast, the IMT calculation, based on the weak-coupling description, results in $h_1 \approx 0.24$ and $h_2 \approx 0.38$, as shown in Fig. 1(b) for comparable model parameters (as discussed in Sec. II). This is a narrower window of h than what is found from RIMT. The possibility of correlation-induced enhancement of the FFLO phase in the parameter space is exciting in the context of strongly correlated systems.

Our investigation on the origin of this enhancement suggests that a subtle balance among relevant energy scales plays the most crucial role. In particular, the intricate interplay between components of the total mean-field energy
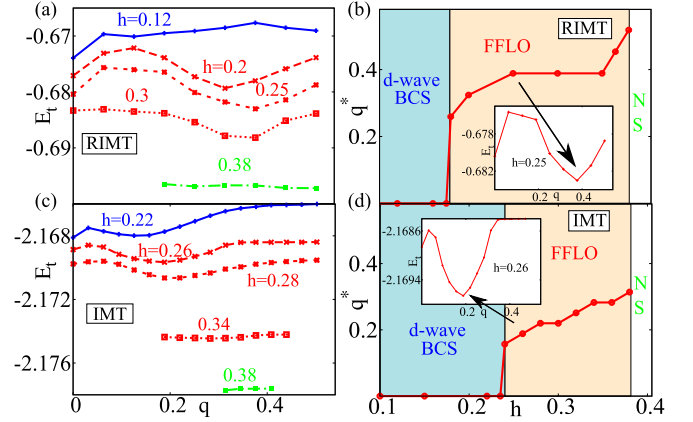
FIG. 2. Determination of q^*, the optimal modulation wave vector of the pairing amplitude, versus h, from RIMT (a) and IMT (c) calculations. The h dependence of q^* from RIMT and IMT findings is shown in panels (b) and (d), respectively. For small h, $E_t(q)$ achieves the minimum for $q = 0$, indicating a uniform BCS d-wave ground state. On the other hand, $E_t(q)$ features a minimum at finite q^* for $0.18 \leqslant h \leqslant 0.38$ in RIMT calculations in panel (a), and for $0.22 \leqslant h \leqslant 0.38$ in plain IMT calculations in panel (c), signaling an FFLO ground state. For large $h > h_2$, the energy minimum is lost and the d-wave pairing amplitude becomes feeble, indicating the collapse of FFLO phase. The evolution of q^* with h is strongly sublinear, with apparent saturation at large h within the RIMT scheme (b), whereas its dependence is approximately linear in IMT calculations (d). The insets in the panels (b) and (d) focus on the energy landscapes with respect to q for specific $h = 0.25$ in panel (b) and $h = 0.26$ in panel (d) within the FFLO region in RIMT and IMT, respectively.

E_t ($= \langle \psi_0 | \mathcal{H}_{GA} | \psi_0 \rangle$) corresponding to the the pairing amplitude (the pairing energy E_p), the spin imbalance (the magnetic energy E_m), and the hopping of electrons (the kinetic energy E_K) decides the window of the FFLO phase. All
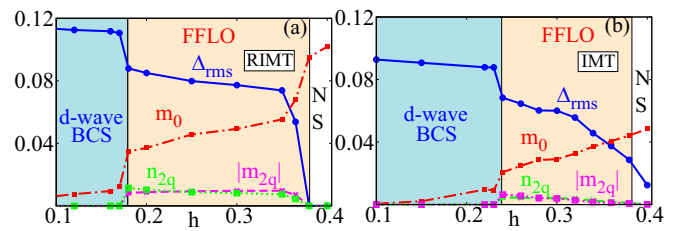
FIG. 3. Evolution of different order parameters as a function of h, obtained from (a) RIMT and (b) IMT calculations. The primary orders shown here are root-mean-square pairing amplitude Δ_{rms} (blue curves), average magnetization m_0 (red curves), and the intertwined SDW m_{2q} (magenta curves) and CDW n_{2q} (green curves) orders (defined in Sec. III B), all presented at $q = q^*(h)$. In d-wave BCS regime Δ_{rms} remains nearly constant and m_0 is small. The onset of FFLO regime at h_1 [$h_1 = 0.18$ and 0.25 in panels (a) and (b)] is signaled by a sharp fall of Δ_{rms} and a steep rise in m. These two orders keep decreasing and increasing in the FFLO regime, with a much slower rate in RIMT results than in IMT. The exit from FFLO regime to NS at h_2 ($h_2 = 0.38$ in both panels) is signaled by a near vanishing of Δ_{rms} while m_0 reaches its normal-state value. The self-generated orders m_{2q} and n_{2q} survive only in the FFLO regime and are stronger in RIMT results than in IMT findings.

of these components are renormalized by the GRFs (also see the discussions in the next paragraph). We note that within the FFLO regime the nature of spatial modulation of the superconducting pairing amplitude and magnetization changes from a stripe modulation at the lower range of h to a checkerboard pattern at the higher h side of the FFLO phase, as highlighted in the insets of Fig. 1. Here, stripe implies a unidirectional modulation with $\mathbf{q} = \pm q(1, 0)$, whereas the checkerboard modulation with wave vector $\mathbf{q}$ is identified with an equal superposition of modulations with $\pm q(1, 0)$ and $\pm q(0, 1)$. This transformation of the nature of modulation is consistent with the earlier calculations [20] on a square lattice. We find this transition from stripe to checkerboard modulation to occur at $h = 0.25$ in RIMT findings (inset of Fig. 1) and at $h = 0.33$ in the IMT method [inset of Fig. 1(b)]. We also mention here that although the main panels of Fig. 1 present results obtained on a much larger system of size 200×200, the results in the insets highlighting the transition in the modulation pattern are solved on a system size of 40×40. This results in a weaker energy resolution compared to the curves presented in the main panel. A smaller system size for the checkerboard pattern of modulation is needed due to its reduced translational symmetry.

In order to develop a deeper understanding of the change of phase boundaries between RIMT and IMT results, we note that both E_m and E_K of the total energy E_t lead to an energy gain in the FFLO phase as h is increased. In contrast, the spatially modulated pairing amplitude results in an energy loss, when compared to a homogeneous BCS state. It is this fine balance between these gains and losses of energy that dictates the boundaries between different phases as h increases. On the other hand, the prohibition of double occupancy through Gutzwiller factors in RIMT renormalizes the separate components of energy differently, and hence it is natural that the aforementioned balance will occur for different h values in RIMT and IMT calculations. We have elaborated this aspect quantitatively in Appendix C to provide a comprehensive picture.

As discussed already, the FFLO phase is characterized by a spatially modulating pairing amplitude and magnetization. It is crucial to decide the correct modulation wave vector. Other than possibilities for the different natures of modulations (consistent with the square symmetry of the underlying lattice), e.g., stripe and checkerboard patterns as discussed already, we also determine the optimal magnitude of q^* by variationally minimizing the total energy E_t of the FFLO state over the entire range of q. This is illustrated in Figs. 2(a) and 2(b), where $E_t(q)$ curves are presented (considering stripe pattern of modulation) using RIMT and IMT calculations respectively. Representative h values in Fig. 2 are chosen from each of BCS, FFLO, and spin-polarized NS. We find for very small $h \ll h_1$ that $E_t(q)$ has a minimum value at $q = 0$. For $h \lesssim h_1$, a second minimum in $E_t(q)$ emerges at a finite q^*, although $E_t(q^*) \gtrsim E_t(q = 0)$. In the FFLO phase for $h_1 \leqslant h \leqslant h_2$, however, $E_t(q)$ develops a global minimum at q^*.

The value of q^* is expected to increase [13,94,97] with h. A larger q^* ensures a larger number of nodes in the spatial profile of the pairing amplitude causing more domain walls. These domain walls support the magnetization arising from h.

Hence, with increasing h, the FFLO state gains more energy by increasing domain wall density. As a result, q^* increases with h. Our results, however, establish that the nature of this rise is different in RIMT and IMT calculations. While q^* follows an apparent sublinear increase in RIMT method as in Fig. 2(c), it rises approximately linearly in IMT results as seen in Fig. 2(d). In RIMT, q^* increases rapidly for $h \gtrsim h_1$ and then gets saturated in a large part of the FFLO window. This is because of an increased role of the effective repulsive energy between domain walls at higher h. In RIMT, Δ undergoes a rapid change of magnitude and sign across narrow domain walls, particularly at small h (for reasons discussed in Sec. III B). Hence, the effective repulsion between the domain walls has little role when their density is small near h_1. However, at large h, the increased effective repulsion between these domain walls does not allow their density to rise as much for large h, leading to a near-saturation of q^*. In contrast, the qualitative behavior of q^* in IMT agrees well with the previous studies [13]. Here, the profile of the pairing amplitude is sinusoidal in the entire FFLO window, and the role of effective repulsion remains weak in the entire FFLO regime, which results in an approximately linear $q^*(h)$.

In addition to the variational determination of q^* outlined above, the energetics of the FFLO, the BCS (i.e., $q = 0$), and the underlying spin-polarized NS are compared to identify the true GS, for each value of h. The q resolution of our calculation is enhanced as we have exploited the translational symmetry of the FFLO phase across the lattice as mentioned earlier in Sec. II and solve the eigensystem of Eq. (17) for $\mathcal{H}_{\mathrm{MF}}$ in the momentum space for a large system. This yields good precisions for the individual components of energy.

B. Order parameters

The phase diagram in Fig. 1 identifies the boundaries between distinct phases, whereas the energy minimum at q^* decides the stability of the broken-symmetry GS. The different energy scales in each of these states and their behavior with h are characterized by the h dependence of various order parameters characterizing our system. With this motivation, we study in Fig. 3 the behavior of the root-mean-square pairing amplitude (Δ_{rms}), average magnetization (m_0), and self-generated intertwined SDW (m_{2q}) and CDW (n_{2q}) orders as a function of h. The Δ_{rms} takes a value Δ_0 in the homogeneous BCS state and $\sqrt{2}\Delta_q$ in the FFLO state. Here,

$$\Delta_{Q_p} = \frac{1}{4N} \sum_k [\langle c_{-k+Q_p\downarrow} c_{k\uparrow} \rangle_0 \eta_k + \langle c_{-k+Q_p\downarrow} c_{k\uparrow} \rangle_0 \eta_{-k+Q_p}],$$
(21)

$$m_Q = \sum_\sigma \frac{\sigma n_Q^\sigma}{2}, \quad n_Q = \sum_\sigma n_Q^\sigma,$$
(22)

where $Q_p = 0$ or q, $Q = 0$ or $2q$, and $\eta_k = 2[\cos(k_x) - \cos(k_y)]$ is the d-wave form factor. Here, n_Q^σ is defined in the text following Eq. (8). The behavior of different order parameters is contrasted from the two calculations: RIMT and IMT. For all h, the average magnetization m_0 attains a higher value in RIMT, as seen in Fig. 3(a). This is due to the reduced bandwidth upon prohibition of double occupancy. The superconducting order parameter is also found stronger in RIMT;
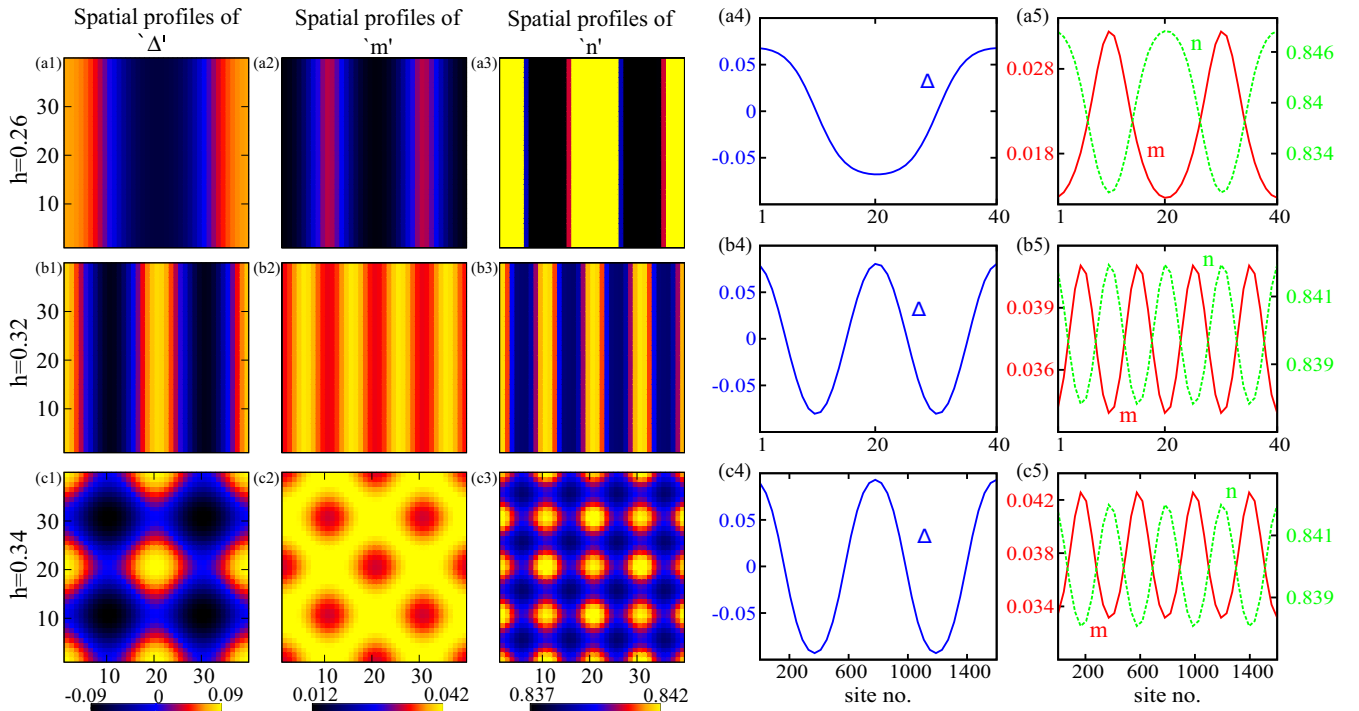
FIG. 4. Evolution of the spatial profiles of order parameters [see Eqs. (4) and (6) and the text following Eq. (7) for definitions] in the FFLO phase from IMT calculations. The spatial profiles are featured in a 3×3 panel on the left side using color-density plots. The evolution of Δ is shown in the left column with h increasing from top to bottom. Similarly, magnetization m and accompanying CDW order are shown in the middle and right columns, respectively. The wavelength of the stripe modulation decreases with increasing h from 0.26 to 0.32, and finally leads to a checkerboard pattern at a higher field ($h = 0.34$). The line plots on the right side provide a cross-sectional view of these profiles along the $\hat{x}$ direction for stripe ($h = 0.26, 0.32$) and along the $\hat{x} + \hat{y}$ direction for checkerboard ($h = 0.34$) modulation.

see Fig. 3. This is because of our choice of exchange coupling J in the Hamiltonian in Eq. (2) in the two methods of calculation to obtain the same value of superconducting energy gap at $h = 0$ in the RIMT and IMT methods. The energy gap and the pairing amplitude differ in RIMT calculations as they obtain different Gutzwiller renormalization. The m_0 and Δ_{rms} calculated within the RIMT scheme experience little change with h, inside the FFLO region (up to $h \approx 0.36$, a value close to h_2), as depicted in Fig. 3(a). These order parameters reach their NS values with further increase in h. Such behavior of the order parameters is related to the saturation of q^* for a wide window of h, followed by a quick change of q^* near h_2 within the FFLO region (see Fig. 2). The order parameter values largely depend on q^*. For a given q^*, increasing h causes only little changes in the order parameters. In IMT, these orders change continuously across the FFLO regime, finally attaining their NS values beyond h_2. The magnitudes of the coexisting SDW (m_{2q}) and CDW (n_{2q}) orders, which are self-generated due to the modulated pairing amplitude, even though they have small values, also increase with strong correlations.

Having understood the behavior of the global order parameters, we next focus on their spatial profiles for different values of h. The self-consistent spatial structure of modulating pairing amplitude, magnetization, and charge density are depicted in color-density plots on the left side in Fig. 4 and Fig. 5 from IMT and RIMT schemes, respectively, whereas the cuts on the right side emphasize the one-dimensional modulations. The panels from top to bottom present results for

increasing h. These results are obtained using real-space BdG simulations carried out on a system of size 40×40. We find from Fig. 4 that the wavelength of the stripe modulations of all three order parameters from IMT calculations decrease as h is increased from $h = 0.26$ to $h = 0.32$. The corresponding wavelength is inversely proportional to the pairing momentum of the Cooper pairs. In the RIMT scenario, however, the wavelength of stripe modulation changes marginally by going from $h = 0.18$ to $h = 0.26$, which is roughly consistent with the weak dependence of q^* on h within the FFLO regime in the RIMT scheme, as shown in Fig. 2, also discussed earlier in Sec. III A. The magnetization m nucleates near the location of nodes of the superconducting pairing amplitude Δ; thus the modulating wavelength of magnetization becomes half of the superconducting pairing amplitude. The modulation in local density n also has this same wavelength.

In the RIMT scenario, Δ goes through a sharp fall where it changes sign. This is because strong electronic repulsions act to suppress the nanoscale density fluctuations locally causing a relatively smooth variations in the spatial density which in turn flattens the small-scale variations in the superconducting pairing amplitude self-consistently in the lattice [86–88]. As a result, the magnitudes of the higher-order modes in the superconducting pairing amplitude and the density modulation increase in a self-consistent manner. These factors make a steeper spatial variation of the superconducting pairing amplitude Δ, where it changes sign in the presence of strong correlations as depicted in Fig. 5, panels (a1) and (a4), compared to that from the IMT outcomes as shown in Fig. 4,
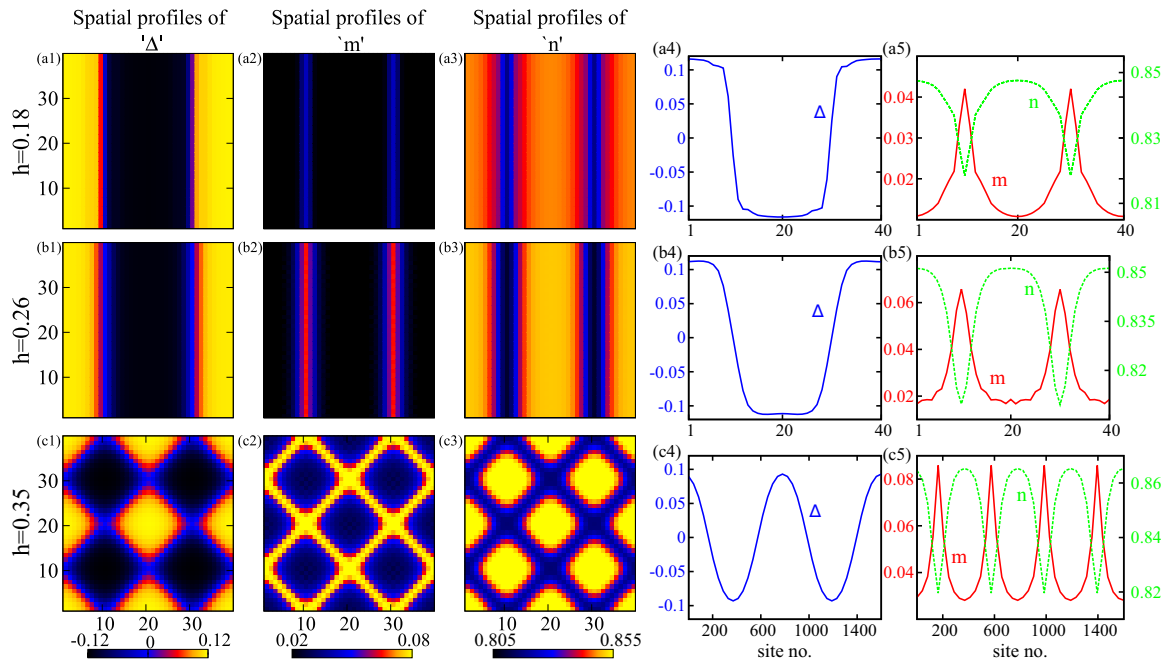
FIG. 5. Evolution of spatial profiles of order parameters [see Eqs. (4) and (6) and the text following Eq. (7) for definitions] in the FFLO phase, similar to Fig. 4 but from RIMT calculations, is shown to emphasize the role of strong repulsive correlations here. The line plots on the right provide cross-sectional view of the order parameter profiles along the $\hat{x}$ direction for stripe ($h = 0.18$, $h = 0.26$) and along the $\hat{x} + \hat{y}$ direction for checkerboard ($h = 0.35$) modulation. The spatial profiles here are obtained from our real-space calculations in a 40×40 lattice system. Note the sharp rise and fall of orders across the line of zero of Δ (discussed in Sec. III D) and the robustness of the wavelength of modulation of the order parameters with increasing h, consistent with our momentum-space findings in Fig. 2(c).

panels (a1) and (a4). This leaves a narrower space for local m to nucleate compared to what is found from the IMT method. The sharpness of the fall of Δ in RIMT, however, reduces with increasing h, reflecting a reduction in the dominance of strong correlations in higher fields. We note that within the FFLO phase, the superconducting order parameter with an extended s-wave symmetry develops near regions in which the d-wave order parameter becomes zero. However, its amplitude remains negligible enough to not make any changes in our qualitative and quantitative findings. We have elaborated more on the possibility of self-consistently obtaining the extended s-wave pairing amplitude in Appendix B.

C. Renormalized parameters

The distinctive features associated with the global and local properties of the order parameters at different values of h are dictated by the renormalized parameters in the Hamiltonian. The mean-field Hamiltonian in Eq. (7) can be recast in terms of the renormalized parameters using the form

$$\mathcal{H}_{\mathrm{MF}} = \sum_{i,\alpha,\sigma} -t_{\mathrm{eff}}^{\sigma}(i,\alpha)(\hat{c}_{i\sigma}^{\dagger}\hat{c}_{i+\alpha\sigma} + \mathrm{H.c.}) + \sum_{i,\sigma} \mu_{\mathrm{eff}}^{\sigma}(i)\hat{c}_{i\sigma}^{\dagger}\hat{c}_{i\sigma}$$

$$+ \text{pairing terms involving } \Delta_{i\uparrow}^{\alpha}, \Delta_{i\downarrow}^{\alpha}. \quad (23)$$

The explicit expressions of $t_{\mathrm{eff}}^{\sigma}(i)$ and $\mu_{\mathrm{eff}}^{\sigma}(i)$ can be obtained by comparing Eq. (7) with Eq. (23). The major contribution in $t_{\mathrm{eff}}^{\sigma}$ in RIMT comes from the GRF for hopping, $g^{t\sigma}$ ($= 0.275$ at $\langle n \rangle = 0.84$, when $h = 0$), which restricts the hopping solely to the unoccupied sites. Strong correlations also induce spin dependence in the hopping parameters at finite h. At finite h, the number of sites occupied by the down-spin species

decreases in the lattice. Thus the up-spin electrons find it easier to hop around and vice versa (assuming up-spin is favored by h), also reflected in the expressions of $g^{t\sigma}$ in Eq. (A2). We show in Fig. 6 the evolution of renormalized hopping parameter $t_{\mathrm{eff}}^{\sigma} = \sum_{i,\alpha} t_{\mathrm{eff}}^{\sigma}(i,\alpha)$ as a function of h. The reduced t_{eff} (≈ 0.4 at $h = 0$), and thereby the reduced bandwidth and the spin dependence of $t_{\mathrm{eff}}^{\sigma}$, enhances the average magnetization in RIMT calculations. Within the IMT framework, on the other hand, the renormalization of the hopping parameter ($t_{\mathrm{eff}} \approx 1.13$ at $h = 0$) and its spin dependence is negligible, as seen in Fig. 6(b), arising only from the Fock shifts in $\mathcal{H}_{\mathrm{MF}}$. The externally applied magnetic field h also gets renormalized to an effective magnetic field h_{eff} [$= \sum_{i\sigma} \sigma \mu_{\mathrm{eff}}^{\sigma}(i)/2$] in both RIMT and IMT by Hartree shifts of $\mathcal{H}_{\mathrm{MF}}$, defined in Eq. (7). The variation of h_{eff} with respect to the external field h is depicted in Figs. 6(c) and 6(d) from the RIMT and IMT methods, respectively. The suppression is significant in RIMT due to the additional action of $\phi_{i\sigma}$, i.e., the derivatives of GRFs, e.g., $(dg^{J,z}/dn)$, consumed within $\mu_{\mathrm{eff}}^{\sigma}$ in RIMT calculations. $t_{\mathrm{eff}}(i)$ locally plays a key role in homogenizing small-scale inhomogeneities in the spatial profiles of the densities of the system [87].

D. Density of states

Another key feature of a superconducting state is its single-particle density of states (DOS), which carries specific signatures when h is turned on. In order to explore the effects of correlations on the DOS, we study it at different values of h within the RIMT and IMT schemes. The spin-resolved DOSs are evaluated using BdG eigenvalues $\{E_{n\sigma}\}$ and eigenvectors
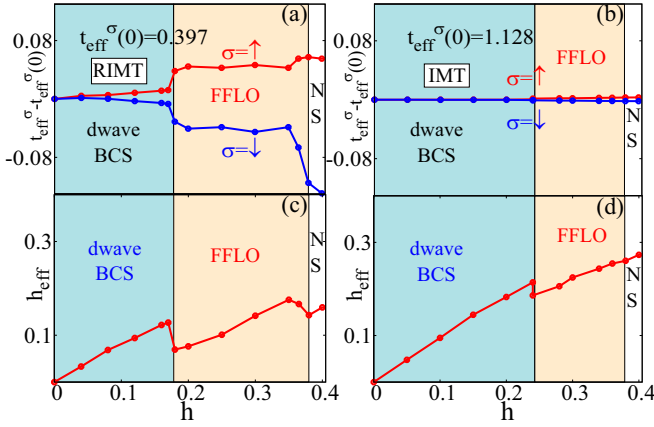
FIG. 6. Behavior of the effective hopping parameter t_{eff} [subtracting $t_{\text{eff}}(h = 0)$] versus h from RIMT (a) and IMT (b) findings. The h dependence of the effective magnetic field h_{eff} from RIMT (c) and IMT (d) outcomes. The strong correlations in panel (a) cause up- and down-spin hopping (denoted by red and blue curves, respectively) to branch out weakly in the BCS regime, while their difference rises sharply in the FFLO phase. The difference increases strongly again upon exiting FFLO phase into NS. In contrast, the up- and down-spin hoppings maintain nearly identical value across the entire range of h within the IMT method (the weak difference is only due to Fock shifts). The behavior of h_{eff} follows a linear trend with bare h in both RIMT (c) and IMT (d) findings for all h. The RIMT calculation results in a somewhat lower h_{eff} in the BCS region and significantly lower h_{eff} in the FFLO and NS region compared to IMT results. h_{eff} faces jumps at h_1 in both RIMT and IMT calculations—the jump being more significant in RIMT. h_{eff} also undergoes a weak jump near h_2 in RIMT, unlike in IMT, where only a continuous change in h_{eff} across h_2 is found.

$\{u_{i,n\sigma}, \ v_{i,n\sigma}\}$ as

$$N_\sigma(\omega) = \frac{1}{N} \sum_{i,n} g_{ii}^{t\sigma} \{|u_{i,n\sigma}|^2 \delta(\omega - E_{n\sigma}) + |v_{i,n\sigma}|^2 \delta(\omega + E_{n\bar\sigma})\}.$$

(24)

The DOSs characterizing different phases obtained by tuning h from the RIMT and IMT methods are shown in Fig. 7 in the left and right columns, respectively. For the d-wave BCS state at a low h ($< h_1$), the DOSs of the two spin flavors split; the up-spin DOS gets shifted towards the left and the down-spin towards the right with respect to the Fermi level by an amount of h_{eff} as shown in Figs. 7(a) and 7(b).

For intermediate magnetic fields $h_1 \leqslant h < h_2$, the FFLO state is identified by a midgap peak [20,32] appearing at $\omega = \mp h_{\text{eff}}$ for up- and down-spin DOSs respectively. This is because the paired states in the FFLO phase reside near the Zeeman-split Fermi surfaces and the single-particle states, which cause finite magnetization, occupy the energies in between them. In real space, the single-particle states are piled up at the zeros of the superconducting pairing amplitude Δ, where it changes sign, and form domain walls. The nearly "square-wave" nature of the Δ modulation within RIMT, as seen in Fig. 5, supports domain walls within narrow regions in real space. The resulting spatial profile of m thus features strong peaks at these narrow domain walls. Such strong
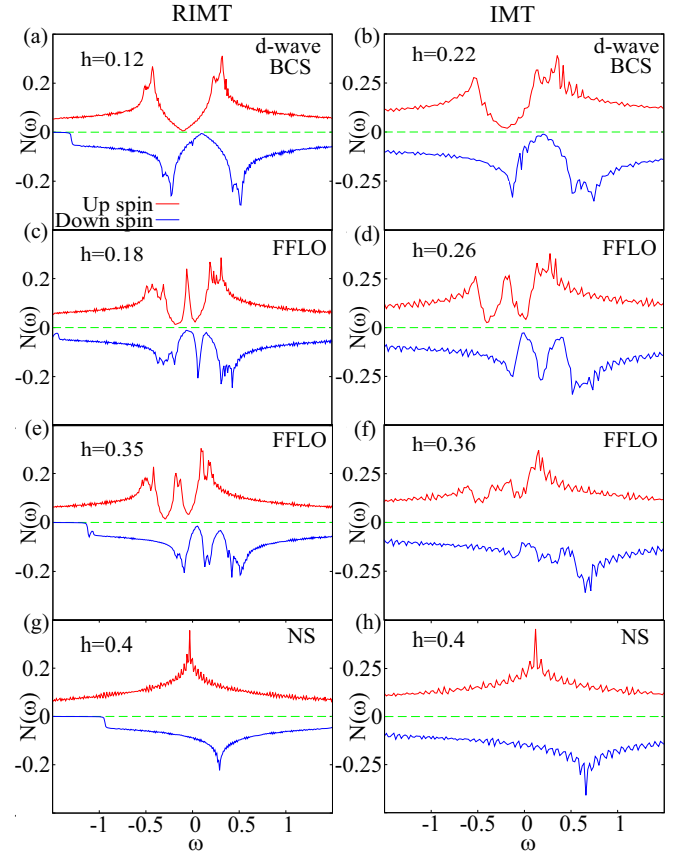
FIG. 7. Spin-resolved average DOS from RIMT (left column) and IMT methods (right column). Panels (a) and (b) show DOS for d-wave BCS state, featuring standard profile where up- and down-spin DOSs are oppositely shifted in energy from Fermi level by h_{eff}. Panels (c) and (d) present DOS in the FFLO phase close to corresponding h_1 highlighting the signature of a bound state through the midgap peak. Notice that the presence of strong correlations makes the midgap peak much sharper in panel (c) compared to IMT outcome in panel (d). Further increase of h deep inside FFLO regime in panels (e) and (f) begins to broaden and subsequently split the midgap peak. Finally, for $h > h_2$ pairing amplitude collapses altogether as seen in panels (g) and (h), and the resulting DOS features standard profile of tight-binding electrons in the presence of a magnetic field in the normal state.

localization of the single-particle states leads to a rather sharp midgap feature in the resulting density of states from RIMT calculations, as seen in Fig. 7(c). These midgap states and the corresponding midgap peak in DOS are reminiscent of the bound states formed due to the Andreev reflections along the nodal lines of a superconductor. Note that the superconducting order parameter changes its sign on the nodal line. The nature of modulation of pairing amplitude in the IMT scheme, however, maintains near-sinusoidal form (higher harmonics less relevant) and as a result, the midgap feature in the corresponding density of states is much less sharp, as can be seen from Fig. 7(b).

As h increases, the domain walls get closer to each other with increasing q^*. This facilitates stronger hybridization of the Andreev bound states, resulting in a broader bandwidth of the midgap peak. In IMT, q^* increases continuously with
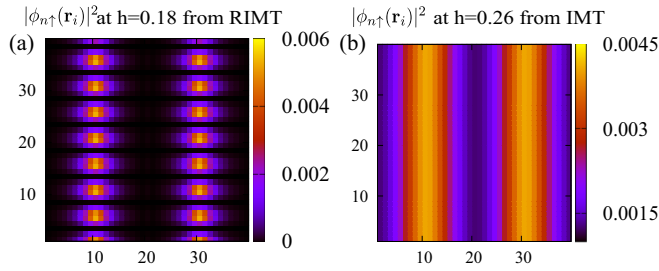
FIG. 8. Spatial distribution of the low-lying wave function $|\phi_n(\mathbf{r}_i)|^2 \equiv |u_{i,n\uparrow}|^2 + |v_{i,n\uparrow}|^2$ for $E_n \approx -h_{\text{eff}}$ to illustrate its bound-edness. Panel (a) demonstrates that $|\phi_n(\mathbf{r}_i)|^2$ at $h = 0.18$ is a more tightly bound state in RIMT calculations than in plain IMT result for $|\phi_n(\mathbf{r}_i)|^2$ in panel (b) for $h = 0.26$. Note that the lack of tight boundedness in the IMT wave function leads to a relatively broader midgap peak in DOS, e.g., in Fig. 7(d).

h within the FFLO region. As a result, the broadening of the midgap peak happens continuously with increasing h and the single-particle states in the midgap peak become unbounded at higher h values, as shown in Fig. 7(f) [94]. However, in RIMT, the midgap states remain bounded even at high h values [see Fig. 7(e)] as a result of the q^* saturation over a range of h.

The sharpness of the midgap feature of DOS in the RIMT results, particularly at lower magnetic fields at $h = 0.18$ in Fig. 7(c), is also due to the reduction of bandwidth to $8t_{\text{eff}}$ ($t_{\text{eff}} \approx 0.4$ at $h = 0$). This reduction further becomes spin-dependent in the presence of h, as shown in Fig. 6(a). The reduced bandwidth also makes the DOS better resolved with closely spaced energy levels in RIMT.

The sharp change of the pairing amplitude and sign near the zeros in RIMT results makes the wave function corresponding to the midgap energy far more localized near the domain walls compared to the IMT findings. This is shown for the lowest-lying wave function $|\phi_n(\mathbf{r})|^2$ (here, $E_n \approx -h_{\text{eff}}$) in Figs. 8(a) and 8(b) from the RIMT and IMT calculations, respectively, to highlight their contrast. The boundedness of the low-lying wave functions reduces as the steepness of the Δ modulation decreases with the increase in h.

E. Fate of FFLO phase in the presence of competing order

Our results in the previous subsections illustrate how an application of Zeeman field h generates an FFLO state from a pristine d-wave superconducting GS (for $h = 0$). One of the hallmarks of most strongly correlated superconductors is that they often carry translational-symmetry-broken orders in their GS—for example, charge orders [98,99] and antiferro-magnetism [100,101] in cuprate superconductors, and spin-density wave (SDW) order in heavy-fermion superconductors [76,77] and Fe-based superconductors [102,103]. Motivated by this, we consider a broken-symmetry GS with d-wave superconducting order and a commensurate SDW order [104] at $h = 0$ and scan the phase space traced by h. The SDW order is often found in strongly correlated superconductors at small doping values. We begin with the Hamiltonian in Eq. (3), and its spin rotational symmetry gets broken by the SDW order even at $h = 0$.
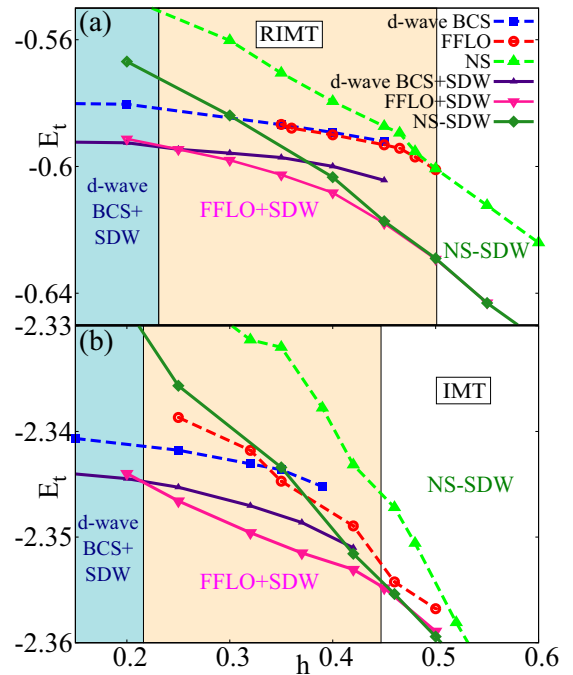
FIG. 9. Energetics of the proposed competing phases with dif-ferent broken symmetries, calculated within RIMT (a) and IMT (b) methods. We consider the d-wave BCS state (blue dashed curves), the FFLO phase (red dashed curves), the normal state (green dashed curves), a state with both the d-wave BCS order and a competing SDW order with (π, π) modulation (dark blue curves), a state with FFLO modulation + competing SDW order with (π, π) modulation (pink curves), and a normal state with (π, π) SDW order (dark green curves) as the possible candidates for comparison, from which the true GS emerges as the one with minimum energy at the given h. The state with FFLO modulation with SDW order (pink shade) is realized as the GS between d-wave BCS + SDW state for low h and the normal state at large h with both RIMT and IMT schemes. This phase is realized for a range of $h_1 \approx 0.23$ to $h_2 \approx 0.45$ in RIMT findings (a), and from IMT (b) window of $h_1 \approx 0.2$ to $h_2 \approx 0.43$.

For this calculation, we fix $\langle n \rangle = 0.9$. With this average density, we focus on addressing the following question: can a translational-symmetry-breaking SDW order in the GS at $h = 0$ perturb the modulating pairing amplitude in the FFLO phase at finite h? The phase diagrams including SDW order using the RIMT and IMT schemes are shown in Figs. 9(a) and 9(b), respectively. Here, we allow the following competing states to emerge at different h values: the d-wave BCS state, a state with the d-wave BCS order coexisting with the SDW order (d-wave BCS + SDW), the FFLO state, a state with an FFLO modulation coexisting with the SDW order (we coin this the FFLO + SDW state), a normal state (NS) with spin imbalance, and the NS with the SDW order (NS-SDW). The FFLO + SDW phase carries an SDW order with a wave vector $(\pi, \pi) - \epsilon$ and an FFLO-like modulation in the paring ampli-tude with $\mathbf{q} \parallel \epsilon$. Here, $\epsilon = (\epsilon, 0)$, where ϵ is a small number. A similar state has recently been studied in Ref. [105]. The final energetics at BdG self-consistency determines the true GS.

We compare the phase diagrams including the competing SDW order for both IMT and RIMT calculations. For a
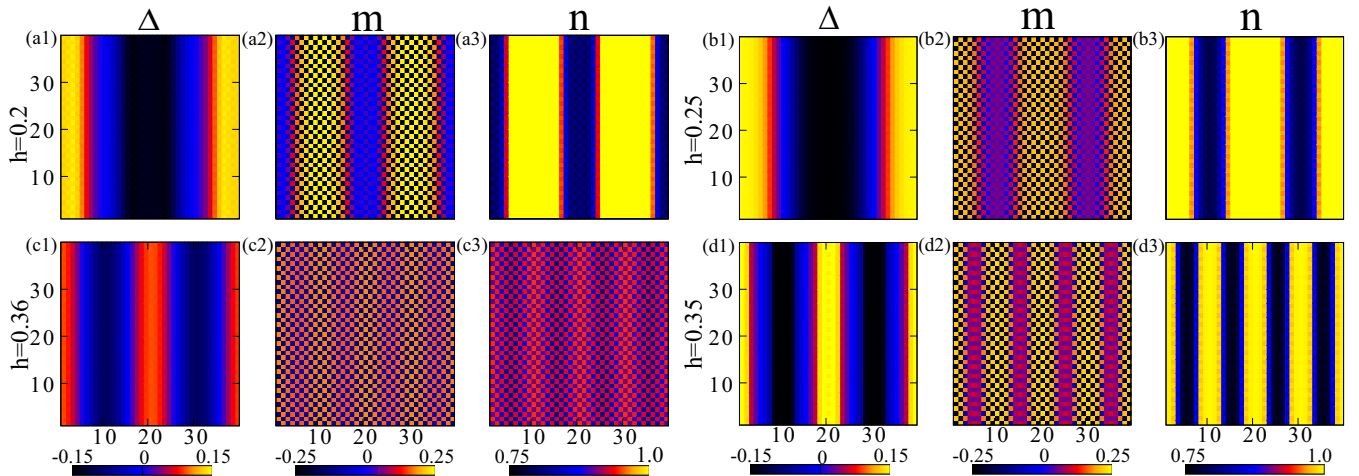
FIG. 10. Evolution of the spatial profiles of different order parameters [see Eqs. (4) and (6) and the text following Eq. (7) for definitions] with h, with a ground state that features a competing SDW order along with the d-wave superconducting order and at $h = 0$, for the chosen set of model parameters, as mentioned in Sec. III E. The 2×3 panels with color-density plots show the spatial profiles of superconducting pairing amplitude (left panels), magnetization (middle panels), and charge density (right panels) on the left side for $h = 0.2$ (top panels) and $h = 0.36$ (bottom panels) obtained from plain IMT calculations. The 2×3 right-side panels are similar depictions from RIMT calculations for $h = 0.25$ and $h = 0.35$, respectively.

legitimate comparison, we fix $J \approx 1.47$ in IMT calculations. This fetches the same d-wave pairing gap in the presence of this SDW order at $h = 0$ in RIMT and IMT. The phases in the GS and the phase boundaries, as obtained from the energetics, are shown in Fig. 9. The calculation for the case with strong correlation is done in a 40×40 lattice, yielding weaker q resolution than our results obtained in momentum space on systems of size 200×200. Our crucial finding from this study is that the GSs for all h, shown in Fig. 9, are essentially those obtained in Fig. 1, but in addition accommodate the competing SDW order, as we discuss below. Note that while the SDW order is put in by hand at $h = 0$, it survives in the self-consistent GS for all h in both RIMT and IMT, as shown in panels (a) and (b) of Fig. 9.

We find that the d-wave BCS + SDW state (dark blue curves) and the NS-SDW state (dark green curves) are always energetically favorable over the FFLO state (red curves) generated from the pristine d-wave superconducting state in both RIMT and IMT, as shown in Fig. 9. However, we further find that the FFLO + SDW state energetically survives for a window of h in the phase diagram. The spatial modulations of different order parameters are shown in Fig. 10 on the left side with IMT results, and on the right side with RIMT results. The upper and lower panels correspond to two strengths of h. The FFLO + SDW state turns out to be the lowest-energy state sandwiched between the d-wave BCS + SDW (at low $h \lesssim h_1$) and NS-SDW (at high $h \gtrsim h_2$) states. In the RIMT scheme, the FFLO + SDW phase ranges from $h_1 \approx 0.23$ to $h_2 \approx 0.45$, and in IMT this region ranges from $h_1 \approx 0.2$ to $h_2 \approx 0.43$. The balances of energy gain and loss from the individual components of the total energy deciding the boundaries of the FFLO + SDW phase for the RIMT and IMT schemes are shown in Fig. 13 in Appendix C. In fact, this window in h in which FFLO + SDW is the ground state appears wider compared to the window in which FFLO was energetically

favorable if SDW order was ignored (as shown in Fig. 1) for both the RIMT and IMT calculations.

Thus, our "toy" calculation indicates that the signature of modulating pairing amplitude, i.e., the impression of FFLO, survives with competing orders in the corresponding GS at $T = 0$.

IV. CONCLUSION

In conclusion, we have studied the effects of strong electronic correlations in the FFLO state of a d-wave superconductor. Thus our results are of great relevance for the search of FFLO signatures in strongly correlated d-wave superconductors, such as CeCoIn$_5$ and the cuprates. Our findings indicate that the strong correlations renormalize all relevant energy scales, whose intricate balance decides the phase space for the FFLO state. Consequently, we found an increased window of the magnetic field for the FFLO phase. We make definitive predictions for the behaviors of the order parameters, pairing momenta, and DOS; all feature interesting distinctions between RIMT and IMT findings. In RIMT, the modulating wave vector of the pairing amplitude rises sharply from zero near the lower critical field and remains nearly saturated over a large part of the FFLO phase. A near saturation of the modulating wave vector of a magnetic order with respect to an external magnetic field has been observed in the Q phase of CeCoIn$_5$ [44]. Had this Q phase been similar to the FFLO state, this near saturation in the modulation of the magnetic order would imply a near saturation of the pairing-amplitude modulation—a feature consistent with our findings. However, the spatial modulation of the magnetic order can arise from other considerations as well [71–73], unrelated to the FFLO phase. Strong interactions were found to homogenize small-scale variations in the Δ landscape, which cause it to change sign rather sharply near $\Delta = 0$. This, in turn, localizes

a high density of Andreev bound states on these domain walls, leading to a narrow and sharp midgap peak in the density of states of the FFLO phase within RIMT. This is consistent with the recent nuclear magnetic resonance experiment on CeCu$_2$Si$_2$, which is suggestive of the presence of a high density of Andreev bound states in its inhomogeneous superconducting state in Zeeman fields [46].

A natural question might arise: Why do we not encounter the FFLO phase in strongly correlated superconductors, e.g., high-T_c cuprate superconductors? In our calculations, we have not included the orbital effect of the applied field in our analysis and considered only the Zeeman effect. In reality, it is challenging to disentangle the orbital and Zeeman effect of an applied field. In particular, for cuprate superconductors, the orbital effect produces vortices at weaker field strengths ($H_{c_2}^{\mathrm{orb}} \sim 100$ T for YBCO near the optimal doping [106]) compared to the Clogston-Chandrasekhar limit ($H_p \sim 170$ T for YBCO (within BCS theory) near the optimal doping [62]), where the Zeeman effect becomes crucial. Thus, it is quite possible that homogeneous superconductivity might become completely disordered, preempting FFLO modulations due to the proliferation of vortices.

On the other hand, Pauli-limited superconductors possessing large Maki parameters [29] (>1.8), which also are strongly correlated, such as heavy-fermion superconductors CeCoIn$_5$, CeCu$_2$Si$_2$, and some of the organic superconductors, show signatures of the FFLO phase, when exposed to a magnetic field. We also have not included the effects of quantum phase fluctuations in either of our recipe: IMT and RIMT. It will be interesting to explore the effects of quantum phase fluctuation on the FFLO physics, particularly at lower doping where the strong correlation effects are significant.

ACKNOWLEDGMENTS

APPENDIX A: OBTAINING RENORMALIZED MEAN-FIELD HAMILTONIAN $\mathcal{H}_{\mathrm{MF}}$ OF EQ. (7)

1. Detailed expressions for GRFs used in Eq. (3) [107,108] as functions of the order parameters defined in Eqs. (4), (5), (6)

In the process of handling the constraint of strong onsite repulsion ($U \gg t$) in the Hubbard model at our starting point in Sec. II, we employed a Gutzwiller projection operator to focus on a restricted Hilbert space, which prohibits all the double occupancies from the system. While this reduces the Hamiltonian in Eq. (1) to that in Eq. (2), standard manipulation demands further simplifications for the implementation of the constraints. One intuitive and elegant (through approximation) way of implementing the constraint is called the Gutzwiller approximation, which actually gets rid of the constraints at the expense of renormalization of the Hamiltonian parameters locally. The resulting Hamiltonian is given in Eq. (3). Here we have the Gutzwiller renormalization factors (GRFs), i.e., all g's are local variables, to be determined self-consistently. The form of such GRFs can be derived from a phase-space argument [109] or from infinite-
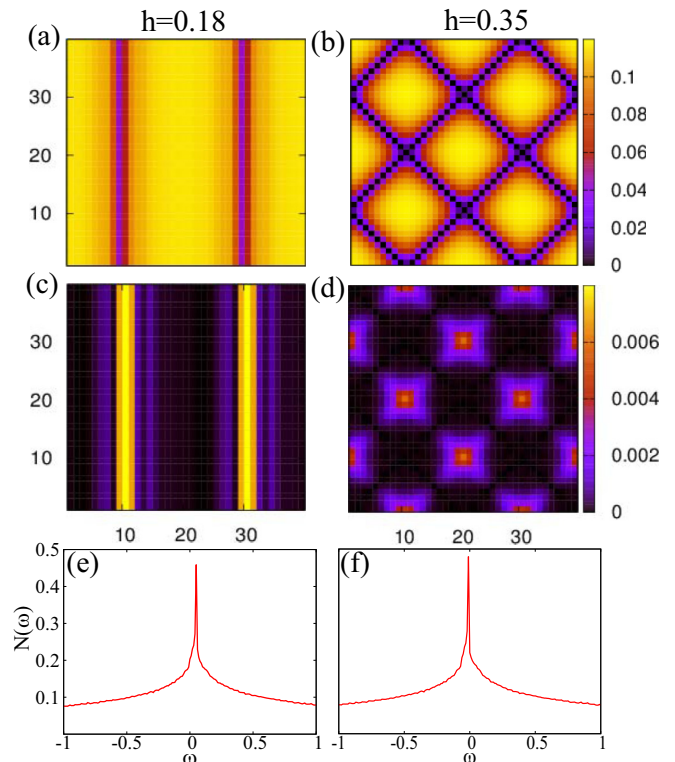
FIG. 11. Spatial profiles of the magnitude of the pairing amplitude with d-wave [panels (a) and (b)] and extended s-wave [panels (c) and (d)] symmetries, shown in the FFLO phase for $h = 0.18$ (left panels) and $h = 0.35$ (right panels) within RIMT calculations. In panels (e) and (f) corresponding average DOSs for up-spin electrons are shown, which are obtained by fully suppressing the d-wave pairing and considering only the self-consistent extended s-wave pairing. The extended s-wave pairing has very small amplitudes in regions where the d-wave pairing in suppressed, and elsewhere it is negligible. In fact, the resulting DOS for both values of h resembles that of the underlying NS of a nearest-neighbor tight-binding model, confirming the irrelevance of the extended s-wave pairing in the FFLO phase.

dimensional calculations [110], and they also depend on the broken-symmetry ground state that we would like our ground state to describe. For our case, we wish to accommodate d-wave superconducting order as well as magnetization in our ground state, and within such premises, the explicit forms of GRFs have been worked out in Ref. [111]. For completeness we list below the expressions of these GRFs in terms of all the order parameters. The GRFs are similar to that used by Ref. [107]:

$$g_{ij}^{t\sigma} = \sqrt{g_i^{t\sigma} g_j^{t\sigma}}, \tag{A1}$$

$$g_i^{t\sigma} = \sqrt{\frac{2\delta_i(1-\delta_i)}{(1-\delta_i^2+4m_i^2)} \frac{1+\delta_i+\sigma 2m_i}{1+\delta_i-\sigma 2m_i}}, \tag{A2}$$

$$g_{ij}^{J,xy} = g_i^{J,xy} g_j^{J,xy}, \tag{A3}$$

$$g_{ij}^{J,xy} = \frac{2\delta_i(1-\delta_i)}{(1-\delta_i^2+4m_i^2)}, \tag{A4}$$

$$g_{ij}^{J,z} = g_{ij}^{J,xy} \frac{2(\Delta_{ij}^2 + \tau_{ij}^2) - 4m_i m_j X_{ij}^2}{2(\Delta_{ij}^2 + \tau_{ij}^2) - 4m_i m_j}, \tag{A5}$$

$$X_{ij}^2 = 1 + \frac{12(1 - \delta_i)(1 - \delta_j)(\Delta_{ij}^2 + \tau_{ij}^2)}{\sqrt{(1 - \delta_i^2 + 4m_i^2)(1 - \delta_j^2 + 4m_j^2)}}. \tag{A6}$$

Here, $\delta i = 1 - n_i$, where $n_i = \sum_\sigma n_{i\sigma}$, $\Delta_{ij} = \sum_\sigma \Delta_{ij\sigma}/2$, $\tau_{ij} = \sum_\sigma \tau_{ij\sigma}/2$.

2. Details of mean-field decomposition of $\mathcal{H}_{t-J}$ defined in Eq. (2)

The method of derivation of the mean-field Hamiltonian of nature as given in Eq. (7) starting from the bare Hamiltonian like in Eq. (3) is standard and can be found in the literature [87]. Here, we proceed to describe the procedure specifically for our investigation of the FFLO state, for the sake of completeness.

We minimize $\langle \psi_0 | \mathcal{H}_{GA} | \psi_0 \rangle$ with respect to $|\psi_0\rangle$ (Sec. II), under the constraints of fixed total electron density

$N^{-1} \sum_i n_i = \langle n \rangle$ and normalization of the wave function $\langle \psi_0 | \psi_0 \rangle = 1$, or equivalently we minimize the functional $W = \langle \psi_0 | \mathcal{H}_{GA} | \psi_0 \rangle - \lambda(\langle \psi_0 | \psi_0 \rangle - 1) - \mu(\sum_i n_i - \langle n \rangle)$ as follows:

$$\mathcal{H}_{MF} = \sum_{\langle ij \rangle \sigma} \frac{\partial W}{\partial \tau_{ij\sigma}} (\hat{c}_{i\sigma}^\dagger \hat{c}_{j\sigma} + \text{H.c.}) + \sum_{i\sigma} \frac{\partial W}{\partial n_{i\sigma}} \hat{n}_{i\sigma}$$
$$+ \sum_{\langle ij \rangle \sigma} \frac{\partial W}{\partial \Delta_{ij\sigma}} \sigma \hat{c}_{i\sigma} \hat{c}_{j\overline{\sigma}}, \tag{A7}$$

which leads to the renormalized mean-field Hamiltonian $\mathcal{H}_{MF}$ of Eq. (7).

3. Expressions of $\xi_{k+Q,\sigma}^{(r)}$ and $\Delta_{k,-k+Q_p}^{(r)}$ of Eq. (11)

For the periodic and clean system we have considered, $\mathcal{H}_{MF}$ in Eq. (7) can be best solved in momentum space after performing Fourier transformation, as obtained in Eq. (11). Here, we present the detailed expressions $\xi_{k+Q\sigma}^{(r)}$ and $\Delta_{k,-k+Q_p}^{(r)}$ appearing in Eq. (11):

$$\xi_{k+Q\sigma}^{(r)} = - \sum_{\alpha = \pm\hat{x}, \pm\hat{y}} (g_{Q\alpha}^{t\sigma} + \Gamma_{Q\sigma}^\alpha) e^{i\mathbf{k}\cdot\alpha} + \frac{J}{4}[(g_0^{J,z} - 1)n_Q^\sigma - (g_0^{J,z} + 1)n_Q^{\overline{\sigma}}]\gamma_Q + \frac{J}{2} \sum_{Q', \alpha' = \hat{x}, \hat{y}} (g_{Q'-Q,\alpha'}^{J,z})(n_{Q'}^\sigma - n_{Q'}^{\overline{\sigma}}) \cos(\mathbf{Q}\cdot\alpha')$$

$$- \frac{J}{2} g_0^{J,xy} \tau_Q^{\overline{\sigma}} \gamma_{k+Q} - J \sum_{Q'\alpha'} g_{Q'-Q,\alpha'}^{J,xy} \tau_{Q',\alpha'}^{1\overline{\sigma}} \cos[(\mathbf{k}+\mathbf{Q})\cdot\alpha'] - J \sum_{Q'\alpha'} g_{Q'-Q,\alpha}^{J,xy} \tau_{Q',\alpha'}^{2\overline{\sigma}} \sin[(\mathbf{k}+\mathbf{Q})\cdot\alpha'] - \frac{J}{4}(g_0^{J,z} - 1)\tau_Q^\sigma \gamma_{k+Q}$$

$$- \frac{J}{2} \sum_{Q'\alpha'} g_{Q'-Q,\alpha'}^{J,z} \tau_{Q',\alpha'}^{1\sigma} \cos[(\mathbf{k}+\mathbf{Q})\cdot\alpha'] - \frac{J}{2} \sum_{Q'\alpha'} g_{Q'-Q,\alpha'}^{J,z} \tau_{Q',\alpha'}^{2\sigma} \sin[(\mathbf{k}+\mathbf{Q})\cdot\alpha'] + \phi_{Q\sigma} - \mu_\sigma, \tag{A8}$$

$$\Delta_{k,-k+Q_p}^{(r)} = - \frac{J}{2} g_0^{J,xy} \Delta'_{Q_p} \eta_{-k+Q_p} - \frac{J}{4}(g_0^{J,z} + 1)\Delta'_{Q_p} \eta_k - J \sum_{Q'_p,\alpha'} (g_{Q_p-Q'_p,\alpha'}^{J,xy})\Delta_{Q'_p,\alpha'}^{1'} \cos[(\mathbf{k}-\mathbf{Q_p})\cdot\alpha']$$

$$- J \sum_{Q'_p\alpha'} (g_{Q_p-Q'_p,\alpha'}^{J,xy})\Delta_{Q'_p,\alpha'}^{2'} \sin[(\mathbf{k}-\mathbf{Q_p})\cdot\alpha'] - \frac{J}{2} \sum_{Q'_p\alpha'} (g_{Q_p-Q'_p,\alpha'}^{J,z})\Delta_{Q'_p,\alpha'}^{1'} \cos[(\mathbf{k}-\mathbf{Q_p})\cdot\alpha']$$

$$- \frac{J}{2} \sum_{Q'_p\alpha'} (g_{Q_p-Q'_p,\alpha'}^{J,z})\Delta_{Q'_p,\alpha'}^{2'} \sin[(\mathbf{k}-\mathbf{Q_p})\cdot\alpha'] - \sum_{\alpha'} \theta_{Q_p\uparrow}^{\alpha'} \cos[(\mathbf{k}-\mathbf{Q_p})\cdot\alpha'] - \sum_{\alpha'} \theta_{Q_p\downarrow}^{\alpha'} \cos(\mathbf{k}\cdot\alpha'). \tag{A9}$$

Here,

$$\tau_Q^\sigma = \frac{1}{4N} \sum_k \langle \hat{c}_{k\sigma}^\dagger \hat{c}_{k-Q,\sigma} \rangle_0 \gamma_k,$$

$$\tau_{Q,\alpha'}^{1\sigma} = \frac{1}{N} \sum_k \langle \hat{c}_{k\sigma}^\dagger \hat{c}_{k-Q,\sigma} \rangle_0 \cos(\mathbf{k}\cdot\alpha'),$$

$$\tau_{Q,\alpha'}^{2\sigma} = \frac{1}{N} \sum_k \langle \hat{c}_{k\sigma}^\dagger \hat{c}_{k-Q,\sigma} \rangle_0 \sin(\mathbf{k}\cdot\alpha'); \tag{A10}$$

$$\Delta'_{Q_p} = \frac{1}{4N} \sum_k \langle \hat{c}_{-k+Q_p\uparrow}^\dagger \hat{c}_{k\downarrow}^\dagger \rangle_0 \eta_k,$$

$$\Delta_{Q_p,\alpha'}^{1'} = \frac{1}{N} \sum_k \langle \hat{c}_{-k+Q_p\uparrow}^\dagger \hat{c}_{k\downarrow}^\dagger \rangle_0 \cos(\mathbf{k}\cdot\alpha'),$$

$$\Delta_{Q_p,\alpha'}^{2'} = \frac{1}{N} \sum_k \langle \hat{c}_{-k+Q_p\uparrow}^\dagger \hat{c}_{k\downarrow}^\dagger \rangle_0 \sin(\mathbf{k}\cdot\alpha'), \tag{A11}$$

where $Q' = 0, \pm 2q, \pm 4q$, $Q'_p = \pm q, \pm 3q$, $\gamma_k = 2[\cos(k_x) + \cos(k_y)]$, $\eta_k = 2[\cos(k_x) - \cos(k_y)]$, $n_Q^\sigma = N^{-1}\langle \hat{c}_{k\sigma}^\dagger \hat{c}_{k-Q,\sigma} \rangle_0$, and $g_{Q\alpha}^{t\sigma}$, $g_{Q\alpha}^{J,xy}$, $g_{Q\alpha}^{J,z}$, $\Gamma_{Q\sigma}^\alpha$, $\theta_{Q_p\sigma}^\alpha$, $\phi_{Q\sigma}$ are Fourier modes of $g_{i\alpha}^{t\sigma}$, $g_{i\alpha}^{J,xy}$, $g_{i\delta}^{J,z}$, $\Gamma_{i\sigma}^\alpha$, $\theta_{i\sigma}^\alpha$, $\phi_{i\sigma}$, respectively.

APPENDIX B: POSSIBILITY OF EXTENDED *s*-WAVE SYMMETRY IN PAIRING AMPLITUDE

The *t*-*J* model can, in principle, give rise to anisotropic pairing amplitude in both *d*-wave and extended *s*-wave channels. However, within our parameter regime, the strength of the extended *s*-wave component is very weak—essentially zero in both RIMT and IMT results—in the absence of orbital field, i.e., $h = 0$. Therefore, we start (at $h = 0$) with a pure *d*-wave homogeneous state. When this phase becomes spatially modulated in the FFLO regime at a finite h ($h_1 \leqslant h \leqslant h_2$), a weak extended *s*-wave symmetry is induced in regions where the *d*-wave pairing amplitude vanishes due to modulations,
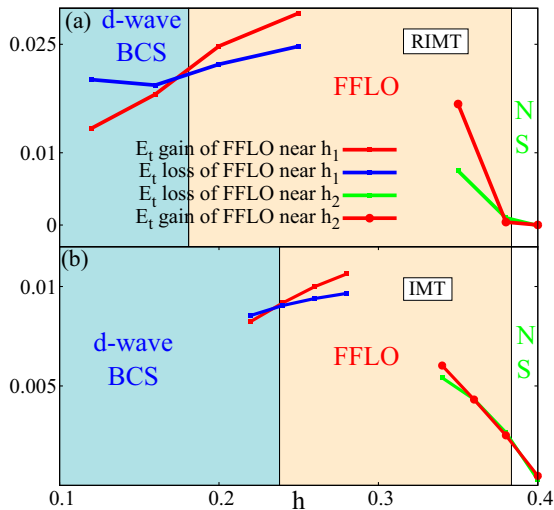
FIG. 12. Differences of the components of E_t near the phase boundaries (h_1 and h_2) as a function of h in RIMT (a) and IMT (b) methods. The shaded regions in pink represent the FFLO state. Here, E_t gain of the FFLO equals E_t of the competing phase, such as BCS or NS, minus E_t of the FFLO phase, and E_t loss of the FFLO equals E_t of the FFLO phase minus E_t of the competing phase, such as BCS or NS. E_t gain of the FFLO (red curve near h_1) phase through E_K and E_m crosses the E_t loss of the FFLO (blue curve near h_1) due to E_p with respect to the BCS state at h_1, which occurs early in RIMT. At h_2 the difference of E_t components between FFLO and NS approaches zero. Consequently, E_t gain and E_t loss of FFLO with respect to NS merge with each other at the FFLO-NS boundary.

FIG. 13. Differences of the components of E_t near the phase boundaries as a function of h in RIMT (a) and IMT (b) methods. The shaded regions in pink represent FFLO + SDW state. Here, E_t gain of the FFLO + SDW equals E_t of the competing phase, such as d-wave BCS + SDW or NS-SDW, minus E_t of the FFLO + SDW phase, and E_t loss of the FFLO + SDW equals E_t of the FFLO + SDW phase minus E_t of the competing phase, such as d-wave BCS + SDW or NS-SDW. E_t gain of the FFLO + SDW (black curve near h_1) through E_m crosses the E_t loss of the FFLO + SDW (magenta curve) due to E_p and E_K at h_1, which occurs at 0.23 and 0.2 in RIMT and IMT, respectively. At h_2 the difference of E_t components between FFLO + SDW and NS-SDW approaches zero. Consequently, E_t gain and E_t loss of FFLO + SDW with respect to NS merge with each other at the h_2 boundary, which is ≈ 0.43 and ≈ 0.45 in RIMT and IMT.

as depicted in Figs. 11(a) and 11(b) and in Figs. 11(c) and 11(d) for $h = 0.18$ and $h = 0.35$, respectively. However, the amplitude of this extended s-wave component is negligibly small compared to the d-wave counterpart (maximum value of extended s-wave component is about 10% and 5% of the maximum of d-wave component at $h = 0.18$ and $h = 0.35$, respectively) and it does not affect our qualitative and quantitative conclusions. We have checked this by calculating the average DOS by considering the self-consistency in calculations by allowing only the extended s-wave component of the pairing amplitude and suppressing the d-wave component to zero everywhere. We find that the resulting DOS resembles that of the underlying noninteracting tight-binding model and carries essentially no signature of the extended s-wave pairing, as portrayed in Figs. 11(e) and 11(f). This conclusion remains unaltered in results obtained from IMT calculations as well; we do not show that result explicitly for simplicity.

APPENDIX C: EVOLUTIONS OF THE ENERGY GAIN AND LOSS WITH RESPECT TO THE MAGNETIC FIELD AT THE PHASE BOUNDARIES

Our main result in Sec. III showed that the phase boundaries between BCS, FFLO, and NS move around depending on the inclusion of strong correlations in the fold of the calculation. It was also argued that the signatures of strong correlations renormalize different components of energy in a different manner, such that the subtle balance between these components is achieved at different strengths of the Zeeman

field h, causing the phase boundaries to be different for RIMT and IMT. Here, we illustrate the above statement in the following manner in terms of our results.

The differences of the energy components of the competing phases without the competing SDW order near their phase boundaries with respect to h obtained from the RIMT and IMT schemes are shown in Fig. 12. The pairing energy (E_p) favors a uniform BCS phase over the FFLO phase, because the spatial modulation of the order parameter comes at an energy cost, most easily seen from a Ginzburg-Landau expansion of free energy [1]. In contrast, the magnetization energy (E_m) and effective kinetic energy (E_K) costs are better accommodated in the FFLO phase, because of the nucleation of the E_m and E_K at the domain walls formed along the nodes of Δ in real space in the FFLO phase. Because of the GRFs appearing in the Hamiltonian $\mathcal{H}_{MF}$ in Eq. (11), which are self-consistently determined for specific location in the parameter space, independent components of energies evolve differently with h. As a result, the changeover from BCS to FFLO and subsequently from FFLO to normal state can occur at different h_1 and h_2 in principle, from RIMT and IMT calculations. The crossing of ($E_m + E_K$) gain and E_p loss in the FFLO phase as found at h_1 reduces in RIMT, because the rate of change of energy gain in FFLO due to ($E_m + E_K$) increases compared to the energy loss from E_p near h_1. This is expected because strong correlations homogenize the small-scale variations in Δ in

the FFLO phase and make the zero region of Δ narrower by steepening the fall of Δ nearly the same as depicted in Fig. 5. Therefore, even near a reduced h_1, the FFLO state becomes energetically favorable compared to the BCS state as the loss of E_p in the FFLO state is less compared to the gain in E_m which mainly stems from the increased magnetization due to lowering of bandwidth in RIMT. On the other hand, inside the FFLO region the gap filling, or in other words, the decay of E_p ($E_p \approx 0$ determines h_2), occurs at a relatively slower rate in RIMT due to renormalization of the effective magnetic field h_{eff} as shown in Fig. 6(c), and therefore h_2 does not shift in a fashion similar to that of h_1.

Figure 13 shows the balances in the energy components at the phase boundaries of the competing phases with the competing SDW order from the RIMT and IMT calculations. The competing phases here are d-wave BCS + SDW phase, FFLO + SDW phase, and the underlying normal state. Near h_1, the FFLO + SDW phase is favored by E_m and the d-wave BCS + SDW phase is favored by E_p and E_K. Renormalization of the parameters is due to Gutzwiller factors and as a result of that the renormalized energy components cause different h_1 values in RIMT and IMT. The h_2 in the two cases are also different due to different renormalization of the parameters in RIMT and IMT.

[1] M. Tinkham, *Introduction to Superconductivity*, 2nd ed. (Dover Publications, New York, 2004).

[2] A. M. Clogston, Phys. Rev. Lett. **9**, 266 (1962).

[3] B. S. Chandrasekhar, Appl. Phys. Lett. **1**, 7 (1962).

[4] P. Fulde and R. A. Ferrell, Phys. Rev. **135**, A550 (1964).

[5] A. I. larkin and Y. N. Ovchinnikov, Zh. Eksp. Teor. Fiz. **47**, 1136 (1964) [Sov. Phys. JETP **20**, 762 (1965)].

[6] J. Wårdh and M. Granath, Phys. Rev. B **96**, 224503 (2017).

[7] F. Loder, S. Graser, A. P. Kampf, and T. Kopp, Phys. Rev. Lett. **107**, 187001 (2011).

[8] D. F. Agterberg and H. Tsunetsugu, Nat. Phys. **4**, 639 (2008).

[9] Y. Wang, S. D. Edkins, MD. H. Hamidian, J. C. S. Davis, E. Fradkin, and S. A. Kivelson, Phys. Rev. B **97**, 174510 (2018).

[10] E. Fradkin, S. A. Kivelson, and J. M. Tranquada, Rev. Mod. Phys. **87**, 457 (2015).

[11] D. F. Agterberg, J. C. Séamus Davis, S. D. Edkins, E. Fradkin, D. J. Van Harlingen, S. A. Kivelson, P. A. Lee, L. Radzihovsky, J. M. Tranquada, and Y. Wang, arXiv:1904.09687.

[12] E. Berg, E. Fradkin, S. A. Kivelson, and J. M. Tranquada, New J. Phys. **11**, 115004 (2009).

[13] K. Yang and S. L. Sondhi, Phys. Rev. B **57**, 8566 (1998).

[14] S. Takada and T. Izuyama, Prog. Theor. Phys. **41**, 635 (1969).

[15] Q. Wang, C.-R. Hu, and C.-S. Ting, Phys. Rev. B **74**, 212501 (2006).

[16] B. Jin, G. Su, and Q.-R. Zheng, Phys. Rev. B **73**, 064518 (2006).

[17] Q. Cui and K. Yang, Phys. Rev. B **78**, 054501 (2008).

[18] Y. Yanase and M. Sigrist, J. Phys. Soc. Jpn. **78**, 114715 (2009).

[19] Q. Cui, C.-R. Hu, J. Y. T. Wei, and K. Yang, Phys. Rev. B **85**, 014503 (2012).

[20] T. Zhou and C. S. Ting, Phys. Rev. B **80**, 224515 (2009).

[21] A. V. Samokhvalov, A. S. Mel'nikov, and A. I. Buzdin, Phys. Rev. B **82**, 174514 (2010).

[22] M. M. Maśka, M. Mierzejewski, J. Kaczmarczyk, and J. Spałek, Phys. Rev. B **82**, 054509 (2010).

[23] Y. L. Loh, N. Trivedi, Y. M. Xiong, P. W. Adams, and G. Catelani, Phys. Rev. Lett. **107**, 067003 (2011).

[24] Y. Yanase, New J. Phys. **11**, 055056 (2009).

[25] A. Ptok, K. J. Kapcia, P. Piekarz, and A. M. Oleś, New J. Phys. **19**, 063039 (2017).

[26] K. V. Samokhin and B. P. Truong, Phys. Rev. B **99**, 014503 (2019).

[27] A. Samoilenka, M. Barkman, A. Benfenati, and E. Babaev, arXiv:1905.03774.

[28] K. W. Song and A. E. Koshelev, Phys. Rev. B **97**, 224520 (2018).

[29] D. Saint-James, G. Sarma, and E. J. Thomas, *Type II Superconductivity* (Pergamon Press, Oxford, 1969).

[30] L. G. Aslamazov, Sov. Phys. JETP **28**, 773 (1969).

[31] S. Takada, Prog. Theor. Phys. **43**, 27 (1970).

[32] Y. L. Loh and N. Trivedi, Phys. Rev. Lett. **104**, 165302 (2010).

[33] A. Ptok, Acta Phys. Pol., A **118**, 420 (2010).

[34] T. Tayama, A. Harita, T. Sakakibara, Y. Haga, H. Shishido, R. Settai, and Y. Onuki, Phys. Rev. B **65**, 180504(R) (2002).

[35] H. A. Radovan, N. A. Fortune, T. P. Murphy, S. T. Hannahs, E. C. Palm, S. W. Tozer, and D. Hall, Nature (London) **425**, 51 (2003).

[36] X. Gratens, L. Mendonça Ferreira, Y. Kopelevich, N. F. Oliveira, R. R. Urbano, R. A. Ribeiro, R. Movshovich, J. L. Sarrao, J. D. Thompson, Z. Fisk, and P. G. Pagliuso, Phys. Rev. B **85**, 054502 (2012).

[37] C. Martin, C. C. Agosta, S. W. Tozer, H. A. Radovan, E. C. Palm, T. P. Murphy, and J. L. Sarrao, Phys. Rev. B **71**, 020503(R) (2005).

[38] A. Bianchi, R. Movshovich, C. Capan, P. G. Pagliuso, and J. L. Sarrao, Phys. Rev. Lett. **91**, 187004 (2003).

[39] V. F. Correa, T. P. Murphy, C. Martin, K. M. Purcell, E. C. Palm, G. M. Schmiedeshoff, J. C. Cooley, and S. W. Tozer, Phys. Rev. Lett. **98**, 087001 (2007).

[40] J. Spehling, R. H. Heffner, J. E. Sonier, N. Curro, C. H. Wang, B. Hitti, G. Morris, E. D. Bauer, J. L. Sarrao, F. J. Litterst, and H.-H. Klauss, Phys. Rev. Lett. **103**, 237003 (2009).

[41] K. Kumagai, M. Saitoh, T. Oyaizu, Y. Furukawa, S. Takashima, M. Nohara, H. Takagi, and Y. Matsuda, Phys. Rev. Lett. **97**, 227002 (2006).

[42] G. Koutroulakis, M. D. Stewart, V. F. Mitrović, M. Horvatić, C. Berthier, G. Lapertot, and J. Flouquet, Phys. Rev. Lett. **104**, 087001 (2010).

[43] C. Capan, A. Bianchi, R. Movshovich, A. D. Christianson, A. Malinowski, M. F. Hundley, A. Lacerda, P. G. Pagliuso, and J. L. Sarrao, Phys. Rev. B **70**, 134513 (2004).

[44] M. Kenzelmann, T. Strässle, C. Niedermayer, M. Sigrist, B. Padmanabhan, M. Zolliker, A. D. Bianchi, R. Movshovich, E. D. Bauer, J. L. Sarrao, and J. D. Thompson, Science **321**, 1652 (2008).

[45] S.-Z. Lin, D. Y. Kim, E. D. Bauer, F. Ronning, J. D. Thompson, and R. Movshovich, arXiv:1902.04797.

[46] S. Kitagawa, G. Nakamine, K. Ishida, H. S. Jeevan, C. Geibel, and F. Steglich, Phys. Rev. Lett. **121**, 157004 (2018).

[47] H. Mayaffre, S. Krämer, M. Horvatic, C. Berthier, K. Miyagawa, K. Kanoda, and V. F. Mitrovic, Nat. Phys. **10**, 928 (2014).

[48] G. Koutroulakis, H. Kühne, J. A. Schlueter, J. Wosnitza, and S. E. Brown, Phys. Rev. Lett. **116**, 067003 (2016).

[49] S. Uji, Y. Iida, S. Sugiura, T. Isono, K. Sugii, N. Kikugawa, T. Terashima, S. Yasuzuka, H. Akutsu, Y. Nakazawa, D. Graf, and P. Day, Phys. Rev. B **97**, 144505 (2018).

[50] S. Uji, K. Kodama, K. Sugii, T. Terashima, Y. Takahide, N. Kurita, S. Tsuchiya, M. Kimata, A. Kobayashi, B. Zhou, and H. Kobayashi, Phys. Rev. B **85**, 174530 (2012).

[51] P. J. W. Moll, J. Kanter, R. D. McDonald, F. Balakirev, P. Blaha, K. Schwarz, Z. Bukowski, N. D. Zhigadlo, S. Katrych, K. Mattenberger, J. Karpinski, and B. Batlogg, Phys. Rev. B **84**, 224507 (2011).

[52] J. A. Wright, E. Green, P. Kuhns, A. Reyes, J. Brooks, J. Schlueter, R. Kato, H. Yamamoto, M. Kobayashi, and S. E. Brown, Phys. Rev. Lett. **107**, 087002 (2011).

[53] C. C. Agosta, J. Jin, W. A. Coniglio, B. E. Smith, K. Cho, I. Stroe, C. Martin, S. W. Tozer, T. P. Murphy, E. C. Palm, J. A. Schlueter, and M. Kurmoo, Phys. Rev. B **85**, 214514 (2012).

[54] K. Cho, B. E. Smith, W. A. Coniglio, L. E. Winter, C. C. Agosta, and J. A. Schlueter, Phys. Rev. B **79**, 220507(R) (2009).

[55] R. Lortz, Y. Wang, A. Demuer, P. H. M. Böttger, B. Bergk, G. Zwicknagl, Y. Nakazawa, and J. Wosnitza, Phys. Rev. Lett. **99**, 187002 (2007).

[56] R. Beyer, B. Bergk, S. Yasin, J. A. Schlueter, and J. Wosnitza, Phys. Rev. Lett. **109**, 027003 (2012).

[57] S. Sugiura, T. Isono, T. Terashima, S. Yasuzuka, J. A. Schlueter, and S. Uji, npj Quantum Mater. **4**, 7 (2019).

[58] C.-w. Cho, J. H. Yang, N. F. Q. Yuan, J. Shen, T. Wolf, and R. Lortz, Phys. Rev. Lett. **119**, 217002 (2017).

[59] D. A. Zocco, K. Grube, F. Eilers, T. Wolf, and H. v. Löhneysen, Phys. Rev. Lett. **111**, 057007 (2013).

[60] K. Cho, H. Kim, M. A. Tanatar, Y. J. Song, Y. S. Kwon, W. A. Coniglio, C. C. Agosta, A. Gurevich, and R. Prozorov, Phys. Rev. B **83**, 060502(R) (2011).

[61] H. Burkhardt and D. Rainer, Ann. Phys. **506**, 181 (1994).

[62] J. L. O'Brien, H. Nakagawa, A. S. Dzurak, R. G. Clark, B. E. Kane, N. E. Lumpkin, R. P. Starrett, N. Muira, E. E. Mitchell, J. D. Goettee, D. G. Rickel, and J. S. Brooks, Phys. Rev. B **61**, 1584 (2000).

[63] A. S. Dzurak, B. E. Kane, R. G. Clark, N. E. Lumpkin, J. O'Brien, G. R. Facer, R. P. Starrett, A. Skougarevsky, H. Nakagawa, N. Miura, Y. Enomoto, D. G. Rickel, J. D. Goettee, L. J. Campbell, C. M. Fowler, C. Mielke, J. C. King, W. D. Zerwekh, D. Clark, B. D. Bartram, A. I. Bykov, O. M. Tatsenko, V. V. Platonov, E. E. Mitchell, J. Herrmann, and K.-H. Müller, Phys. Rev. B **57**, R14084 (1998).

[64] K. Yang and D. F. Agterberg, Phys. Rev. Lett. **84**, 4970 (2000).

[65] Y. Matsuda and H. Shimahara, J. Phys. Soc. Jpn. **76**, 051005 (2007).

[66] V. F. Mitrović, M. Horvatić, C. Berthier, G. Knebel, G. Lapertot, and J. Flouquet, Phys. Rev. Lett. **97**, 117002 (2006).

[67] B.-L. Young, R. R. Urbano, N. J. Curro, J. D. Thompson, J. L. Sarrao, A. B. Vorontsov, and M. J. Graf, Phys. Rev. Lett. **98**, 036402 (2007).

[68] D. F. Agterberg, M. Sigrist, and H. Tsunetsugu, Phys. Rev. Lett. **102**, 207004 (2009).

[69] Y. Yanase and M. Sigrist, J. Phys. Soc. Jpn. **80**, 094702 (2011).

[70] Y. Yanase and M. Sigrist, J. Phys.: Condens. Matter **23**, 094219 (2011).

[71] Y. Kato, C. D. Batista, and I. Vekhter, Phys. Rev. Lett. **107**, 096401 (2011).

[72] J. H. J. Martiny, M. N. Gastiasoro, I. Vekhter, and B. M. Andersen, Phys. Rev. B **92**, 224510 (2015).

[73] S. Raymond, S. M. Ramos, D. Aoki, G. Knebel, V. P. Mineev, and G. Lapertot, J. Phys. Soc. Jpn. **83**, 013707 (2014).

[74] C. Petrovic, P. G. Pagliuso, M. F. Hundley, R. Movshovich, J. L. Sarrao, J. D. Thompson, Z. Fisk, and P. Monthoux, J. Phys.: Condens. Matter **13**, L337 (2001).

[75] A. McCollam, S. R. Julian, P. M. C. Rourke, D. Aoki, and J. Flouquet, Phys. Rev. Lett. **94**, 186401 (2005).

[76] T. Hu, H. Xiao, T. A. Sayles, M. Dzero, M. B. Maple, and C. C. Almasan, Phys. Rev. Lett. **108**, 056401 (2012).

[77] A. Bianchi, R. Movshovich, I. Vekhter, P. G. Pagliuso, and J. L. Sarrao, Phys. Rev. Lett. **91**, 257001 (2003).

[78] T. Takenaka, Y. Mizukami, J. A. Wilcox, M. Konczykowski, S. Seiro, C. Geibel, Y. Tokiwa, Y. Kasahara, C. Putzke, Y. Matsuda, A. Carrington, and T. Shibauchi, Phys. Rev. Lett. **119**, 077001 (2017).

[79] G. Pang, M. Smidman, J. Zhang, L. Jiao, Z. Weng, E. M. Nica, Y. Chen, W. Jiang, Y. Zhang, W. Xie, H. S. Jeevan, H. Lee, P. Gegenwart, F. Steglich, Q. Si, and H. Yuan, Proc. Natl. Acad. Sci. USA **115**, 5343 (2018).

[80] B. J. Powell and R. H. McKenzie, J. Phys.: Condens. Matter **18**, R827 (2006).

[81] J. Wosnitza, Crystals **2**, 248 (2012).

[82] K. Izawa, H. Yamaguchi, Y. Matsuda, H. Shishido, R. Settai, and Y. Onuki, Phys. Rev. Lett. **87**, 057002 (2001).

[83] M. Daniel, E. D. Bauer, S.-W. Han, C. H. Booth, A. L. Cornelius, P. G. Pagliuso, and J. L. Sarrao, Phys. Rev. Lett. **95**, 016406 (2005).

[84] A. Vorontsov and I. Vekhter, Phys. Rev. Lett. **96**, 237001 (2006).

[85] B. B. Zhou, S. Misra, E. H. da Silva Neto, P. Aynajian, R. E. Baumbach, J. D. Thompson, E. D. Bauer, and A. Yazdani, Nat. Phys. **9**, 474 (2013).

[86] A. Garg, M. Randeria, and N. Trivedi, Nat. Phys. **4**, 762 (2008).

[87] D. Chakraborty and A. Ghosal, New J. Phys. **16**, 103018 (2014).

[88] S. Tang, E. Miranda, and V. Dobrosavljevic, Phys. Rev. B **91**, 020501(R) (2015).

[89] A. Paramekanti, M. Randeria, and N. Trivedi, Phys. Rev. B **70**, 054504 (2004).

[90] F. C. Zhang, C. Gros, T. M. Rice, and H. Shiba, Supercond. Sci. Technol. **1**, 36 (1988).

[91] W.-H. Ko, C. P. Nave, and P. A. Lee, Phys. Rev. B **76**, 245113 (2007).

[92] M. R. Norman, M. Randeria, H. Ding, and J. C. Campuzano, Phys. Rev. B **52**, 615 (1995).

[93] P. G. de Gennes, *Superconductivity of Metals and Alloys* (W. A. Benjamin Inc., New York, 1966).

[94] A. B. Vorontsov, J. A. Sauls, and M. J. Graf, Phys. Rev. B **72**, 184501 (2005).

[95] A. B. Vorontsov and M. J. Graf, Phys. Rev. B **74**, 172504 (2006).

[96] M. Karmakar and P. Majumdar, Phys. Rev. A **93**, 053609 (2016).

[97] A. Akbari and P. Thalmeier, New J. Phys. **18**, 063030 (2016).

[98] G. Campi, A. Bianconi, N. Poccia, G. Bianconi, L. Barba, G. Arrighetti, D. Innocenti, J. Karpinski, N. D. Zhigadlo, S. M. Kazakov, M. Burghammer, M. v. Zimmermann, M. Sprung, and A. Ricci, Nature (London) **525**, 359 (2015).

[99] Y. Y. Peng, M. Salluzzo, X. Sun, A. Ponti, D. Betto, A. M. Ferretti, F. Fumagalli, K. Kummer, M. Le Tacon, X. J. Zhou, N. B. Brookes, L. Braicovich, and G. Ghiringhelli, Phys. Rev. B **94**, 184511 (2016).

[100] S. Sachdev, Science **336**, 1510 (2012).

[101] X. F. Lu, N. Z. Wang, H. Wu, Y. P. Wu, D. Zhao, X. Z. Zeng, X. G. Luo, T. Wu, W. Bao, G. H. Zhang, F. Q. Huang, Q. Z. Huang, and X. H. Chen, Nat. Mater. **14**, 325 (2014).

[102] J. Schmiedt, P. M. R. Brydon, and C. Timm, Phys. Rev. B **89**, 054515 (2014).

[103] Q. Si, R. Yu, and E. Abrahams, Nat. Rev. Mater. **1**, 16017 (2016).

[104] Y. Yanase and M. Sigrist, J. Phys.: Conf. Ser. **150**, 052287 (2009).

[105] A. Ptok, M. M. Maśka, and M. Mierzejewski, Phys. Rev. B **84**, 094526 (2011).

[106] G. Grissonnanche, O. Cyr-Choinière, F. Laliberté, S. René de Cotret, A. Juneau-Fecteau, S. Dufour-Beauséjour, M.-È. Delage, D. LeBoeuf, J. Chang, B. J. Ramshaw, D. A. Bonn, W. N. Hardy, R. Liang, S. Adachi, N. E. Hussey, B. Vignolle, C. Proust, M. Sutherland, S. Krämer, J.-H. Park, D. Graf, N. Doiron-Leyraud, and L. Taillefer, Nat. Commun. **5**, 3280 (2014).

[107] R. B. Christensen, P. J. Hirschfeld, and B. M. Andersen, Phys. Rev. B **84**, 184511 (2011).

[108] K.-Y. Yang, W. Q. Chen, T. M. Rice, M. Sigrist, and F.-C. Zhang, New J. Phys. **11**, 055053 (2009).

[109] B. Edegger, V. N. Muthukumar, and C. Gros, Adv. Phys. **56**, 927 (2007).

[110] F. Gebhard, Phys. Rev. B **41**, 9452 (1990).

[111] M. Ogata and A. Himeda, J. Phys. Soc. Jpn. **72**, 374 (2003).